②

MEMORANDUM REPORT BRL-MR-3834

AD-A221 711

BRL

PARALLEL NUMERICAL SIMULATIONS OF AXISYMMETRIC PROJECTILE FLOWS USING ZONAL-OVERLAPPED GRIDS

NISHEETH R. PATEL
WALTER B. STUREK

MAY 1990

U.S. ARMY LABORATORY COMMAND

BALLISTIC RESEARCH LABORATORY
ABERDEEN PROVING GROUND, MARYLAND

90 05 12 068

REPORT DOCUMENTATION PAGE

Form Approved
OMB No. 0704-0188

Public reporting burden for this collection of information is estimated to average 1 hour per response, including the time for reviewing instructions, searching existing data sources, gathering and maintaining the data needed, and completing and reviewing the collection of information. Send comments regarding this burden estimate or any other aspect of this collection of information, including suggestions for reducing this burden, to Washington Headquarters Services, Directorate for Information Operations and Reports, 1215 Jefferson Davis Highway, Suite 1204, Arlington, VA 22202-4302, and to the Office of Management and Budget, Paperwork Reduction Project (0704-0188), Washington, DC 20503.

1. AGENCY USE ONLY (Leave blank)	2. REPORT DATE	3. REPORT TYPE AND DATES COVERED
	May 1990	Final, Jul 86-Jul 88

4. TITLE AND SUBTITLE	5. FUNDING NUMBERS
PARALLEL NUMERICAL SIMULATIONS OF AXISYMMETRIC PROJECTILE FLOWS USING ZONAL-OVERLAPPED GRIDS	1L161102AH43 61102A 00 001 AJ

6. AUTHOR(S)

NISHEETH R. PATEL, and WALTER B. STUREK

7. PERFORMING ORGANIZATION NAME(S) AND ADDRESS(ES)	8. PERFORMING ORGANIZATION REPORT NUMBER

9. SPONSORING/MONITORING AGENCY NAME(S) AND ADDRESS(ES)	10. SPONSORING/MONITORING AGENCY REPORT NUMBER
Ballistic Research Laboratory ATTN: SLCBR-DD-T Aberdeen Proving Ground, Maryland 21005-5066	BRL-MR-3834

11. SUPPLEMENTARY NOTES

12a. DISTRIBUTION/AVAILABILITY STATEMENT	12b. DISTRIBUTION CODE
Approved for public release; distribution is unlimited	

13. ABSTRACT (Maximum 200 words) Recent developments in vector and parallel computer architectures provide the potential for achieving greatly enhanced computational speed in the execution of fluid dynamic flow solvers. In order to explore techniques for efficient utilization of these computer architectural features and to develop an improved capability for modeling highly irregular projectile geometries, the development of a zonal Navier-Stokes computational code was undertaken. This report documents the initial development and validation of this code. The code employs a multi-zone overlapped grid technique and utilizes MacCormack's explicit finite-difference numerical algorithm. Parallel execution features are incorporated within the code that permit implementation on both distributed and shared memory multiprocessors. The code has been applied to several challenging test problems, in particular, the application to a ramjet configuration with a highly complex internal flow is discussed in detail. The computational results are compared with experimental measurements. The code has been found to provide for efficient utilization of vector/parallel computer architectures. Also, the zonal flow field topology has proven to be well suited for configurations with irregular geometries.

14. SUBJECT TERMS	15. NUMBER OF PAGES
Computational Aerodynamics, Compressible Flow, Navier-Stokes, and Parallel Computing	58
	16. PRICE CODE

17. SECURITY CLASSIFICATION OF REPORT	18. SECURITY CLASSIFICATION OF THIS PAGE	19. SECURITY CLASSIFICATION OF ABSTRACT	20. LIMITATION OF ABSTRACT
UNCLASSIFIED	UNCLASSIFIED	UNCLASSIFIED	UL

NSN 7540-01-280-5500

Standard Form 298 (Rev. 2-89)
Prescribed by ANSI Std. 239-18
298-102

(THIS PAGE WAS INTENTIONALLY LEFT BLANK)

TABLE OF CONTENTS

DTIC
COPY
INSPECTED
1

Accession For

NTIS GRA&I	☑	
DTIC TAB	☐	
Unannounced	☐	
Justification		

By

Distribution/

Availability Codes

Dist	Avail and/or Special
A-1	

iii

(THIS PAGE WAS INTENTIONALLY LEFT BLANK)

LIST OF FIGURES

LIST OF FIGURES (Continued)

I. INTRODUCTION

The challenge to solve flow problems involving complicated geometries has led to the exploration of zonal grid techniques using finite-difference methods. In the zonal grid approach, the global mesh for a computational domain is generated using different zones separated by common boundaries called zonal boundaries. On the other hand, large memory and substantial CPU time are required for many realistic problems. On a multiprocessor one divides up a program so that many sections of the code can be worked on simultaneously. Since further gain in computational speed of vector processors can only be achieved at high cost as upper limits on signal speed, packaging densities and heat dissipation are being approached, multiprocessors evolved as higher level architectures. The program can be run much more rapidly if the multiprocessor can transmit data between processors, synchronize processors and make global decisions efficiently. Multiprocessor architectures can be generally divided into two categories: (1) global or shared memory; and (2) local or distributed memory. The CRAY X-MP/48 can be considered as an example of a shared memory multiprocessor, while a hypercube can be considered as an example of distributed memory multiprocessor.

The purpose of this report is to document the principals and operation of a computer program that has been developed to solve the flow about complex aerodynamic shapes in a highly efficient manner. The computer code incorporates a parallel algorithm that can effectively utilize a distributed memory multiprocessor architecture and a zonal grid approach that allows one to provide the capability to conveniently accommodate complex boundary shapes.

The code is structured in such a way that the solution method is independent of zone coupling and parallel programming techniques. This allows execution of the code on sequential or vector computers when parallel programming extensions are not invoked. Also, incorporation of appropriate multi-tasking extensions of shared memory multiprocessors allows the code to execute efficiently on shared memory multiprocessors such as the CRAY X-MP/48.

The governing equations in general curvilinear coordinates are discussed in Section II. In Section III, a brief summary of an algebraic grid generator is presented. The solution algorithm, with details of implementation, is described in Section IV. Comments on the implementation of the code and the speed-up achieved through parallel processing on an INTEL IPSC hypercube and a Cray X-MP/48 are given in Section V. The computational code has been exercised for three flow field problems: constant and variable area shock tube; tubular projectile; and ramjet projectile. Examples of computational results are discussed and compared to experimental data in Section VI.

II. THEORETICAL ANALYSIS

The compressible, turbulent Navier-Stokes equations for axisymmetric and two-dimensional flow can be expressed in the following strong conservation form where the dependent variables ρ, u, v, e are mass averaged, with e being the specific total energy, T the temperature, ρ and p being mean density and pressure, respectively, and t is time:

$$\frac{\partial Q´}{\partial t} + \frac{\partial E´}{\partial x} + \frac{\partial F´}{\partial y} + \left(\frac{F´}{y} + \frac{H´}{y}\right) \beta = 0 \qquad (1a)$$

where

$$Q´ = \begin{bmatrix} \rho \\ \rho u \\ \rho v \\ \rho e \end{bmatrix} \qquad\qquad E´ = \begin{bmatrix} \rho u \\ \rho u u + p - \tau_{xx} \\ \rho u v - \tau_{xy} \\ (\rho e + p)u - \tau_{xx}u - \tau_{xy}v + \dot{q}_x \end{bmatrix}$$

$$F´ = \begin{bmatrix} \rho v \\ \rho u v - \tau_{xy} \\ \rho v v + p - \tau_{yy} \\ (\rho e + p)v - \tau_{xy}u - \tau_{yy}v + \dot{q}_y \end{bmatrix} \qquad (1b)$$

$$H´ = \begin{bmatrix} 0 \\ 0 \\ -p + \sigma_+ \\ 0 \end{bmatrix}$$

$$\tau_{xx} = -2/3 \, (\mu + \epsilon) \, \underset{\sim}{\nabla} \cdot \underset{\sim}{V} + 2(\mu + \epsilon) \frac{\partial u}{\partial x}$$

$$\tau_{xy} = (\mu + \epsilon) \left(\frac{\partial u}{\partial y} + \frac{\partial v}{\partial x}\right)$$

$$\tau_{yy} = -2/3 \, (\mu + \epsilon) \, \underset{\sim}{\nabla} \cdot \underset{\sim}{V} + 2 \, (\mu + \epsilon) \frac{\partial v}{\partial y}$$

$$\sigma_+ = -2/3 \, (\mu + \epsilon) \, \underset{\sim}{\nabla} \cdot \underset{\sim}{V} + 2 \, (\mu + \epsilon) \frac{v}{y}$$

$$\underset{\sim}{\nabla} \cdot \underset{\sim}{V} = \frac{\partial u}{\partial x} + \frac{\partial v}{\partial y} + \left(\frac{v}{y}\right) \beta$$

$$\dot{q}_x = -C_p \left(\frac{\mu}{Pr} + \frac{\epsilon}{Pr_t}\right) \frac{\partial T}{\partial x}$$

$$\dot{q}_y = -C_p \left(\frac{\mu}{Pr} + \frac{\epsilon}{Pr_t}\right) \frac{\partial T}{\partial y}$$

where μ is molecular viscosity, ε is eddy viscosity and $\beta = 1$ or 0 for axisymmetric or two-dimensional cases, respectively.

The air was assumed to be a perfect gas for both internal and external flows, satisfying the equation state

$$p = \rho RT$$

where R is the gas constant (1716 ft^2/sec^2 - °R for air). For the dependence of laminar viscosity on temperature, Sutherland's law was used:

$$\mu = 2.270 \ \frac{T^{3/2}}{T + 198.6} \times 10^{-8} \ \frac{lb - sec}{ft^2} . \tag{2}$$

The laminar and turbulent Prandtl numbers, Pr and Pr_t, were assumed constant with values of 0.72 and $_{J}$.9, respectively. The ratio of specific heats, γ, was also assumed constant and equal to 1.4. C_v and C_p are specific heat capacities at constant volume and constant pressure, respectively.

($C_v = 4290 \ ft^2/sec^2$ - °R and $C_p = 6006 \ ft^2/sec^2$ - °R for air).

The total energy per unit mass, e, is given by:

$$e = C_v T + (1/2) \ (u^2 + v^2).$$

In the ξ - η computational plane, Equation (1a) is transformed to the conservation law form represented by:

$$\frac{\partial \bar{Q}}{\partial t} + \frac{\partial \bar{E}}{\partial \xi} + \frac{\partial \bar{F}}{\partial \eta} + \frac{1}{Jy} (F' + H')\beta = 0 \tag{3a}$$

where

$$J = \xi_x \eta_y - \xi_y \eta_x \tag{3b}$$

$$U = \xi_x u + \xi_y v$$

$$V = \eta_x u + \eta_y v$$

$$\bar{Q} = \frac{Q'}{J}$$

3

$$\bar{E} = \frac{1}{J} \left(\xi_x E' + \xi_y F' \right)$$

$$\bar{F} = \frac{1}{J} \left(\eta_x E' + \eta_y F' \right) .$$

The governing equations are formed in such a way that either 2-D or axisymmetric flow with inviscid, thin layer Navier-Stokes or full Navier-Stokes options can be chosen. After some algebraic manipulations Equation (3a) can be transformed into the following form:

$$\frac{\partial Q}{\partial t} + \frac{\partial E}{\partial \xi} + \frac{\partial F}{\partial \eta} + \frac{1}{Jy} (F' + H')\beta = \frac{\partial}{\partial \xi} S_1(Q,Q_\xi) + \frac{\partial}{\partial \xi} S_2(Q,Q_\eta) + \frac{\partial}{\partial \xi} G_1$$

$$+ \frac{\partial}{\partial \eta} T_1 (Q,Q_\xi) + \frac{\partial}{\partial \eta} T_2(Q,Q_\eta) + \frac{\partial}{\partial \eta} G_2 \tag{4a}$$

where

$$Q = \frac{1}{J} \begin{bmatrix} \rho \\ \rho u \\ \rho v \\ \rho e \end{bmatrix} \qquad\qquad E = \frac{1}{J} \begin{bmatrix} \rho U \\ \rho u U + \xi_x p \\ \rho v U + \xi_y p \\ (\rho e + p)\ U \end{bmatrix}$$

$$\tag{4b}$$

$$F = \frac{1}{J} \begin{bmatrix} \rho V \\ \rho u V + \eta_x p \\ \rho v V + \eta_y p \\ (\rho e + p)\ V \end{bmatrix} \qquad S_1 = \frac{1}{J} \begin{bmatrix} 0 \\ B_1 u_\xi + B_2 v_\xi \\ B_2 u_\xi + B_3 v_\xi \\ B_1 u u_\xi + B_2(v u_\xi + u v_\xi) + B_3 v v_\xi + B_4 T_\xi \end{bmatrix}$$

$$S_2 = \frac{1}{J} \begin{bmatrix} 0 \\ C_1 u_\eta + C_2 v_\eta \\ C_3 u_\eta + C_4 v_\eta \\ C_1 u u_\eta + C_2 u v_\eta + C_3 v u_\eta + C_4 v v_\eta + C_5 T_\eta \end{bmatrix} \tag{4c}$$

$$T_1 = \frac{1}{J} \begin{bmatrix} 0 \\ C_1 u_\xi + C_3 v_\xi \\ C_2 u_\xi + C_4 v_\xi \\ C_1 u u_\xi + C_2 v u_\xi + C_3 u v_\xi + C_4 v v_\xi + C_5 T_\xi \end{bmatrix}$$

4

$$T_2 = \frac{1}{J} \begin{bmatrix} 0 \\ D_1 u_n + D_2 v_n \\ D_2 u_n + D_3 v_n \\ D_1 u u_n + D_2 (v u_n + u v_n) + D_3 v v_n + D_4 T_n \end{bmatrix}$$

$$G_1 = \begin{bmatrix} 0 \\ -\tfrac{2}{3}(\mu + \epsilon)\,\xi_x\,(v/y) \\ -\tfrac{2}{3}(\mu + \epsilon)\,\xi_y\,(v/y) \\ -\tfrac{2}{3}(\mu + \epsilon)\,\xi_x\,(v/y)u - \tfrac{2}{3}(\mu + \epsilon)\,\xi_y\,(v^2/y) \end{bmatrix}$$

$$G_2 = \begin{bmatrix} 0 \\ -\tfrac{2}{3}(\mu + \epsilon)\,n_x\,(v/y) \\ -\tfrac{2}{3}(\mu + \epsilon)\,n_y\,(v/y) \\ -\tfrac{2}{3}(\mu + \epsilon)\,n_x\,(v/y)u - \tfrac{2}{3}(\mu + \epsilon)\,n_y\,(v^2/y) \end{bmatrix}$$

The coefficients B_i, C_j, D_i ($i = 1, 2 \ldots 4$; $j = 1, 2 \ldots 5$) appearing in the viscous terms of Equation (4c) are defined as follows:

$$B_1 = (\mu + \epsilon)(\xi_y^2 + 4/3\,\xi_x^2)$$

$$B_2 = (\mu + \epsilon)(1/3\,\xi_x\xi_y) \tag{4d}$$

$$B_3 = (\mu + \epsilon)(\xi_x^2 + 4/3\,\xi_y^2)$$

$$B_4 = C_p \left(\frac{\mu}{Pr} + \frac{\epsilon}{Pr_t}\right)(\xi_x^2 + \xi_y^2)$$

$$C_1 = (\mu + \epsilon)(\xi_y n_y + 4/3\,\xi_x n_y)$$

$$C_2 = (\mu + \epsilon)(\xi_y n_x - 2/3\,\xi_x n_y)$$

$$C_3 = (\mu + \epsilon)(\xi_x n_y - 2/3\,\xi_y n_x)$$

$$C_4 = (\mu + \epsilon)(\xi_x n_x + 4/3\,\xi_y n_y)$$

5

$$C_5 = C_p \left(\frac{\mu}{Pr} + \frac{\varepsilon}{Pr_t}\right) (\xi_x \eta_x + \xi_y \eta_y)$$

$$D_1 = (\mu + \varepsilon) (\eta_y^2 + 4/3 \, \eta_x^2)$$

$$D_2 = (\mu + \varepsilon) (1/3 \, \eta_x \eta_y)$$

$$D_3 = (\mu + \varepsilon) (\eta_x^2 + 4/3 \, \eta_y^2)$$

$$D_4 = C_p \left(\frac{\mu}{Pr} + \frac{\varepsilon}{Pr_t}\right) (\eta_x^2 + \eta_y^2) .$$

It should be noted that the viscous terms in Equation (4a) have been split into terms which contain derivatives of flow variables in only one direction (either ξ or η). Vectors G_1 and G_2 represent additional terms due to inclusion of an option for axisymmetric 2-D viscous flow. When the source term $(F' + H')$ and vectors G_1 and G_2 are set to zero, one obtains a planar 2-D formulation. It is interesting to note that Equation (4a) retains a form similar to that of the Cartesian counterpart Equation (1a).

The source term $(F' + H')$ of Equation (4a) can be split into inviscid and viscous terms. The viscous terms in turn can be split into terms involving derivatives in ξ and η directions.

$$(F' + H') = (INVISCID - VISCOUS) \tag{5a}$$

$$INVISCID = \begin{bmatrix} \rho v \\ \rho u v \\ \rho v v \\ (\rho e + p) \, v \end{bmatrix} \tag{5b}$$

$$VISCOUS = \begin{bmatrix} AV_{11} + AV_{21} \\ AV_{12} + AV_{22} \\ AV_{13} + AV_{23} \\ AV_{14} + AV_{24} \end{bmatrix} \tag{5c}$$

where AV_{ij} (i = 1,2 and j = 1,2....4) are defined as follows:

6

$$AV_{11} = 0.0$$

$$AV_{12} = (\mu + \epsilon)\,(\xi_y u_\xi + \xi_x v_\xi) \tag{5d}$$

$$AV_{13} = 2(\mu + \epsilon)\,(\xi_y v_\xi)$$

$$AV_{14} = C_p(\frac{\mu}{Pr} + \frac{\epsilon}{Pr_t})\xi_y T_\xi + (\mu+\epsilon)(4/3\xi_y vv_\xi - 2/3\,\xi_x vu_\xi) + (\mu+\epsilon)(\xi_y uu_\xi + \xi_x uv_\xi)$$

$$AV_{21} = 0.0$$

$$AV_{22} = (\mu + \epsilon)\,(n_y u_n + n_x v_n)$$

$$AV_{23} = 2(\mu + \epsilon)\,(n_y v_n - v/y)$$

$$AV_{24} = C_p(\frac{\mu}{Pr} + \frac{\epsilon}{Pr_t})n_y T_n + (\mu+\epsilon)(4/3n_y vv_n - 2/3n_x vu_n - 2/3v^2/y) + (\mu+\epsilon)(n_y uu_n + n_x uu_n).$$

This completes the derivation of the governing equations which allows a choice between 2-D and axisymmetric cases with inviscid, thin-layer or full Navier-Stokes options.

III. GENERATION OF COMPUTATIONAL GRIDS

As described in Section II, the governing equations have been expressed in terms of general boundary conforming coordinates in order to facilitate the treatment of arbitrary flow configurations. The technique employed in the construction of coordinate systems is based on algebraic transformations. The grid generation code reads in a discrete number of user defined boundary points. The code uses a cubic-spline function to define boundary shapes and an analytic function to distribute the boundary points. The interior grid points are distributed using Vinokur's[1] clustering function based on a hyper-bolic tangent. This clustering function gives smooth changes in grid line spacing and provides sufficient control of grid line spacing at the bound-aries. This grid generation procedure does not provide control over grid line orthogonality. However, the procedure gives the desired degree of flexibility for the problems under consideration. The non-orthogonal feature of the procedure turns out to be beneficial in that the problem is not overly con-strained by the orthogonality condition, which would necessarily destroy boundary conforming grids in areas of sharp or highly concave/convex corners.

Furthermore, the grid distribution in the streamwise and radial directions are independent, allowing desired clustering at all boundaries. Also, the procedure permits the generation of partially clustered and partially uniform grids in either direction. As will be shown later, this feature is useful for some zonal grid overlapping. Two examples which demonstrate the capabilities of this simple grid generation technique are illustrated in Figures 1 and 2. Grid clustering on the right and upper boundaries is shown in Figure 1. An example where clustering is varied in two regions of a zone in the vertical direction and a smooth variation in axial distribution achieved with different left and right increments is shown in Figure 2.

IV. SOLUTION ALGORITHM

1. NUMERICAL PROCEDURE

MacCormack's[2] explicit and unsplit method is utilized for numerical integration of the governing equations (4) in time from an assumed initial condition until a steady solution is obtained. The finite-difference method for the one-dimensional equation:

$$\frac{\partial Q}{\partial t} + \frac{\partial E}{\partial \xi} = 0 \tag{6}$$

is given by the following predictor - corrector steps:

$$\overline{Q_{i,j}^{n+1}} = Q_{i,j}^{n} - \frac{\Delta t}{\Delta \xi} (E_{i,j}^{n} - E_{i-1,j}^{n}) \tag{7a}$$

$$Q_{i,j}^{n+1} = 1/2[Q_{i,j}^{n} + \overline{Q_{i,j}^{n+1}} - \frac{\Delta t}{\Delta \xi}(\overline{E_{i+1,j}^{n+1}} - \overline{E_{i,j}^{n+1}})] \tag{7b}$$

where $\overline{E_{i,j}^{n+1}}$ implies that the terms are evaluated using $\overline{Q_{i,j}^{n+1}}$ and so forth. After completion of the above described two steps, first derivatives of the governing equations are approximated by second-order accurate central differences. As explained in Reference 3, second derivatives of the viscous terms were also effectively centrally differenced.

The reason for using the unsplit method over time-split method is to save the number of accessions of the memory. In other words, for advancing one time-step, the unsplit method requires considerably less access to the memory than the time-split method. For the explicit method the time-step size must not exceed the maximum allowed by the CFL condition. An approximate linearized stability analysis for the inviscid equations yields the following:

$$\Delta t = \frac{1}{\frac{|U|}{\Delta \xi} + \frac{|V|}{\Delta \eta} + c\{(\frac{\xi_x}{\Delta \xi} + \frac{\eta_x}{\Delta \eta})^2 + (\frac{\xi_y}{\Delta \xi} + \frac{\eta_y}{\Delta \eta})^2\}^{1/2}} \tag{8}$$

8

where c is the speed of sound. Since the terms involving molecular and eddy viscosity stabilize the solution, the time-step size computed using the inviscid analysis was found stable for both inviscid and viscous applications. Equation (8) was multiplied by a factor (denoted as CFL) that is slightly less than one.

2. BOUNDARY AND INITIAL CONDITIONS

The boundary conditions for the governing equations can be categorized into five major types - freestream, downstream, wall, symmetric and no-reflection. A schematic illustration of the application of these boundary conditions for a projectile flow field is shown in Figure 3.

The freestream boundary conditions are held at the appropriate freestream values for the duration of the solution procedure. At the downstream boundary, the conventional zero-gradient boundary condition is applied. The flow variables are extrapolated based on the computed interior values. Along the body surface $n(x,y) = 0$ the boundary conditions are:

$$V = 0 \text{ (No transparency)}$$

$$\frac{\partial U}{\partial \eta} = 0 \text{ (Tangency or Slip)} \tag{9}$$

$$\frac{\partial T}{\partial \eta} = 0 \text{ (Adiabatic Wall)}$$

while, for viscous flow the no-slip condition is $U = 0$. The pressure on the body surface can be obtained by applying normal pressure boundary condition.

$$\nabla p \cdot \nabla n = 0 \tag{10}$$

Using the momentum equations, the normal pressure boundary condition is:

$$(\xi_x n_x + \xi_y n_y)p_\xi + (n_x^2 + n_y^2)p_n = \rho[u(n_x)_t + v(n_y)_t]$$
$$- \rho U(n_x u_\xi + n_y v_\xi) \tag{11}$$

The same relation has been used in viscous flow with $U = 0$. the flow properties along the symmetry line ($\eta = 0$) were specified by the no gradient conditions,

$$\frac{\partial \rho}{\partial \eta} = 0$$

$$\frac{\partial u}{\partial \eta} = 0 \tag{12}$$

$$\frac{\partial p}{\partial \eta} = 0$$

in addition to v = 0 being enforced.

9

The fifth category of boundary condition refers to the top boundary $(\eta = \eta_{max})$. This boundary was established as a no reflection boundary. At the top boundary, waves generated in the interaction process in the vicinity of the wall must exit the computational domain. In order to prevent these waves from reflecting from the top boundary back into the computational domain and perhaps contaminating the solution, a no reflection boundary condition was developed. The boundary conditions are:

$$\frac{\partial u}{\partial I} = 0$$

$$\frac{\partial v}{\partial I} = 0$$

$$\frac{\partial \rho}{\partial I} = 0 \tag{13}$$

$$\frac{\partial p}{\partial I} = 0$$

where the derivative $(\partial/\partial I)$ is taken in the direction of the outwards running Mach line. This condition is appropriate if the flow is locally supersonic (i.e., Mach lines exist), and if there is a single family of outward running Mach lines. A description of this boundary condition is given in more detail in Appendix A.

The boundary conditions are implemented in the code using second-order accurate finite-difference approximations in general.

For the present calculations, the initial conditions were prescribed using either the freestream or lower Mach number condition at all grid points in the computational domain. However, when available, previously computed solutions (obtained with different grids, etc.) were employed as initial conditions in subsequent calculations.

3. NUMERICAL DAMPING

Several types of nonlinear instability are encountered in the present calculation. The remedies for these have been discussed by MacCormack.[4] One of them can be removed by adding a fourth-order pressure damping term to the right hand side of the predictor and corrector step. For the ξ direction the following expression is added to the flux $E_{i,j}^{n}$ in the predictor step

$$\alpha \frac{\{|U_{i,j}| + |(\xi_x^2 + \xi_y^2)_{i,j}^{1/2}| c_{i,j}\} \times |p_{i+1,j} - 2p_{i,j} + p_{i-1,j}| \times (Q_{i+1,j} - Q_{i,j})}{(p_{i+1,j} + 2p_{i,j} + p_{i-1,j})}$$

10

where α is a damping constant with values between 0.5 and 5.0. The damping term is of significance only in the vicinity of pressure oscillations. Also, this damping term is more compact than standard fourth-order smoothing terms in that it requires data at just three grid points instead of the usual five points. It will be shown later that, for zonal grids, this feature permits the employment of single grid cell overlap.

4. ZONAL-OVERLAPPED GRIDDING

A multi-zone overlapped gridding technique is used to extend the time dependent procedure to complex geometries. The computational domain is subdivided into several zones, each of which require a relatively simple grid generation technique.

The zonal gridding approach has a number of advantages over conventional wrap around techniques: (1) difficulties in handling sharp corners can be eliminated, as shown in Figure 4; (2) finer grids can easily be used in regions where rapid changes in the flow variables occur; (3) different types of equations, such as the Euler or Navier-Stokes, can be used in different zones. (4) memory storage problems can be conveniently overcome using appropriate data management techniques; and (5) a saving in CPU time can be achieved by discontinuing computations in the converged zones. The information exchange between zones must be consistent with the governing equations and lead to a stable and efficient time marching or iterative scheme. The zonal boundary conditions must be transparent to shocks and regions of flow separation. However, since zonal boundary conditions introduce additional computational overhead, care must be taken to insure that this extra work is significantly less than the overall computational work required by a solution algorithm. Several different techniques for zone coupling are discussed in References 5-8.

A simple zone coupling technique is used in the present work. In this technique zonal grids share one grid cell boundary with geometric continuity of at least one grid cell for overlapped zones. The coupling of zones is obtained by using one grid-cell overlap. This zonal-coupling is simple and transparent to shock-waves and regions of flow separation. The transparency of zonal-coupling is important because the initial conditions are very far from the steady state and, during the transient phase, shocks may travel through the overlapped boundaries. As shown in Figure 5, two zones coincide on a row of overlapped cells. The right-hand side boundary of zone A is contained within zone B and the left-hand side boundary of zone B is contained within Zone A. Since overlapped cells are of the same shape in both zones, this approach requires transfer of information from the field of zone A to the boundary of zone B and vice-versa.

Each multi-zone solution was obtained by taking one time step in each zone and then exchanging boundary information between zones. This zone-coupling technique has been found to be very reliable and accurate. It is a very simple technique and well suited to ballistic projectile configurations. Examples describing the verification of the technique are discussed in Section VI.

11

V. IMPLEMENTATION ON THE HYPERCUBE AND CRAY X-MP/48

The hypercube is an ensemble of homogeneous SISD (Single Instruction Stream, Single Data Stream) or SIMD (Single Instruction Stream, Multiple Data Stream) machines in a loosely coupled (message passing), distributed (local) memory, MIMD (Multiple Instruction Stream, Multiple Data Stream) concurrent processing architecture with a hypercube interconnect topology. The word "hypercube" refers to the specific way they are interconnected. A hypercube is a generalization of the familiar three dimensional cube, and its topology is completely specified by it's "dimension." In general, for a hypercube of dimension "d," there are "2^d" corners, and "d" edges. Each corner of a three dimensional cube is a computer, and each edge is a communication line between the computers at the two corners on each end of the edge. This is known as a three dimensional hypercube (a "d3"). It has eight "nodes" (computers), each with three nearest neighbors and three communication lines to those neighbors.

The INTEL IPSC hypercube is a "d7" with 128 nodes (2^7), and 7 communication lines per node. This hypercube requires an additional computer (cube manager or host) to get programs and data into the hypercube and results out.

A parallel algorithm was developed in such a way that each computational zone can be assigned to a separate node of a hypercube. In addition, all variables for each zone are local so that it can take advantage of the local memory architecture. This allows concurrent computation in each zone on separate hypercube nodes. When required, information can be exchanged between overlapped zones. This was done using separate routines that do zonal coupling and/or synchronization. Most of the parallel programming techniques for local memory architectures such as SEND/RECEIVE are incorporated in these routines.

The Cray X-MP/48 is a shared memory multiprocessor while the hypercube is a distributed memory multiprocessor. Thus, different multi-tasking techniques are required when implementing an algorithm on shared or distributed memory machines. Again, mapping of zones onto processors is an important issue for efficient implementation on shared memory machines. The partitioning across processors for the zonal application can be done in varying degrees of granularity. In a coarse granularity approach, one would map a zone or subregion of a zone on each processor. In general, the approach chosen will depend upon the applications. As number of zones and/or size of zones change from one application to another, the difficulty of uniformly distributing work among the processors may require a new mapping scheme. This load imbalance would result in processors remaining idle until the processor with the largest task completes its portion of the computation. For the eight-zone ramjet problem each zone was assigned to a processor. This was implemented using $ PROCESS and $ ALSO PROCESS directives described by Misegades.[9] In going from one to four processors a speed-up of 2.3 was achieved on the Cray X-MP. In a medium granularity approach, all processors might work on a single zone in parallel. This parallelization consists of decomposing a zone to DO-LOOP level. Since no artificial boundaries are introduced on shared memory machines, this approach generally allows for better load balancing than a coarse granularity approach. On the Cray this can be implemented using microtasking directives such as DO GLOBAL. For the eight-zone ramjet application, this approach achieved speed-up of 3.55 in going from one to four processors. This speed-up

12

could be less than the maximum speed-up that can be obtained for the application because several computations such as boundary conditions and zonal conditions were not done in parallel.

VI. COMPUTATIONAL RESULTS

In order to evaluate the code, a series of test problems were solved. It was necessary to check whether any perturbation was created in the flow field by the use of the zonal boundary conditions. Also, it was necessary to prove that zonal boundaries allow shocks to travel across the interfaces. This was required because, for many applications, the initial conditions are very far from the steady state and, while the solution is converging, shocks travel through the zonal interfaces.

1. CONSTANT AND VARIABLE AREA SHOCK TUBE

A simple constant area shock tube case was considered for inviscid 2-D and axisymmetric flow. The purpose of this initial test case was to evaluate the ability of the zonal boundary technique to pass disturbances across zonal boundaries without creating pertubations in the flow field. The purpose was not to give detailed comparison for a specific pressure ratio in terms of over pressure, etc.; but to compare the output of a single zone case with that of a multi-zone case at every time-step. Multi-zone cases ranging from two zones to 16 zones were considered (Figure 6). The results of each multi-zone test case matched the single zone case bit by bit. No perturbation was found and the shock traveled through the entire computational domain. Next, a variable cross-sectional area shock tube was considered as a test case. The shock tube had a variable diameter driver section, a convergent-divergent nozzle with a diaphram at the throat and a constant area driven section. Again, under the same flow conditions, comparison between the results for a single zone and multi-zone cases (not shown) confirmed the validity of the zonal boundary technique.

2. TURBULAR PROJECTILE AT SUPERSONIC VELOCITIES

In order to evaluate the axisymmetric Navier-Stokes code, the flow in and around a tubular projectile was investigated. The tubular configuration is shown in Figure 7. As shown in Figure 8 the computational domain was subdivided into five overlapped zones. The total grid of 105×30 for the internal flow and 95×24 for the external flow was used for obtaining the solutions. Figures 9a and 9b show the computed Mach number contours for inviscid and viscous solutions, respectively, for the freestream Mach number of 1.7. The Reynolds number is 2.75×10^6 based on chord length for the laminar viscous case. A Schlieren photograph for the same case is shown in Figure 10. In both figures, a strong shock (choked flow) is visible at the leading edge. Figures 11 and 12 show computed Mach contours for inviscid and viscous solutions, respectively, for $M_\infty = 3.5$. Figure 13 shows a Schlieren photograph for the freestream Mach number of 3.5 and Reynolds number 5.67×10^6. For this case, a weak oblique shock is seen at the leading edge. The pressure distribution as a function of axial position along the internal surface for both cases are shown in Figures 14 and 15, respectively. The pressure distribution is about the same for both inviscid and viscous flow. The difference in the

13

pressure distribution between Mach 1.7 and Mach 3.5 can be explained in view of the normal and oblique shock structures in the forebody. For $M_\infty = 3.5$, the pressure rise at the surface, near the exit of the tubular projectile is interesting. This complex behavior can be explained with the help of the Mach contour plot. In the forebody region, an oblique shock generated by the lip of the tubular projectile reflects off the axis. This reflecting shock interacts with flow that is expanding over an inverted wedge corner which is located at the center of the projectile. This shock boundary layer interaction is believed to be responsible for the pressure rise at the surface in the exit region of the tubular projectile. This problem was successfully implemented on the INTEL hypercube multiprocessor.

3. SOLID FUEL RAMJET (SFRJ)

Finally, the flow in and around a solid fuel ramjet (SFRJ) configuration was considered. The design objective for the tubular ramjet powered projectile is to simulate the flight trajectory of a kinetic energy (KE) projectile. A schematic illustration of the SFRJ projectile along with the type of boundary conditions imposed are shown in Figure 16a. The internal configuration of the SFRJ consists of a diverging inlet formed by an axisymmetric cowl followed by a circular injector plate (or flame holder), a combustor and a nozzle. The combustor is located between the injector plate and converging-diverging nozzle. Solid fuel is located along the circular wall of the combustor. The external configuration consists of a tangent-ogive forebody followed by a straight circular afterbody.

A series of wind tunnel tests[10] were initiated in order to provide data to help guide the development of computational modeling techniques for the SFRJ configuration and to provide guidance for the design of a prototype projectile. The wind tunnel test conditions were: freestream Mach Number = 4.0; freestream stagnation pressure = 14.36 psia; and freestream stagnation temperature = 480 R. The experimental data consisted of internal surface pressure measurements and flow visualization.

The objectives of this computational study were to: (1) simulate cold flow inside a standard SFRJ (nozzle diameter 1.54 inches and injector diameter 1.7 inches); (2) simulate a normal shock inlet condition by varying the nozzle throat diameter; and (3) study the internal flow using graphical flow visualization techniques in order to provide a better understanding of the experimentally determined internal surface pressure distributions. Modeling of the combustion process is of interest and will be addressed in the future.

Because of the complex internal geometry which involves several sharp corners, a zonal gridding approach was used. The computational domain was subdivided into eight zones (Figure 16a). In each zone, an algebraic grid was used. A single-cell overlap (Section IV) was used to couple neighboring zones. Preliminary runs with an eight-zone grid indicated sonic flow at the nozzle throat and under-expanded flow at the nozzle exit. Since the flow in the diverging section of the nozzle remained supersonic, the flow in the base area had very little upstream influence. To save CPU time, a substantial number of grid points were removed from zone four and zone seven, and zone eight was totally eliminated. Computations were performed for both Euler and

Navier-Stokes cases. Computational results are discussed below for four different nozzle throat diameters for an injector diameter of 1.7 inches.

Figure 16b shows a seven-zone grid for inviscid computations. The grid is almost uniform in the internal region. The outflow boundaries of zones four and seven were truncated. The grid size for zones one through seven was 15 x 35, 46 x 35, 15 x 21, 26 x 20, 7 x 25, 84 x 30, and 12 x 23, respectively. Inviscid computations for nozzle throat diameters greater than 1.45 showed an internal wall pressure level (P/P_∞) of less than four in both the cowl and combustor regions. As shown in Figure 17, for a nozzle throat diameter of 1.42 inches, the pressure level in the cowl area is close to the wind tunnel measurement (see Figure 20) for a nozzle throat diameter of 1.54 inches. For the wind tunnel measurement, the equivalent nozzle throat diameter is less than 1.54 inches because of the boundary layer displacement thickness. Although the inviscid computation captured the oblique shock and the pressure level in the inlet region quite well, it failed to obtain the measured pressure rise in the combustor. A Mach number contour plot (Figure 17) shows an oblique shock originating just behind the lip of the cowl.

Computations for the nozzle throat diameter of 1.28 inches showed an oscillatory shock behavior. Figures 18a and 18b show a strong oblique shock becoming normal at the cowl lip. However, this normal shock does not remain steady at the cowl lip. This normal shock starts moving out of the cowl and becomes a bow shock (Figures 18c and 18d). Again the bow shock shows unsteady behavior and it becomes a normal shock at the lip and a strong oblique shock. The above described behavior was found cyclic. In other words, the flow keeps going through a cycle of strong oblique to normal to detached bow shock and reversal of the sequence. The flow inside the cowl and combustor is subsonic for the normal and detached bow shock conditions. Existence of oscillatory entry shock phenomena was observed in aerodynamic range tests of a 20mm SFRJ (Reference 11).

Figure 19 shows a seven zone grid used for the Navier-Stokes computations. The grid size for zones one through seven was 20 x 64, 46 x 64, 20 x 25, 64 x 24, 10 x 32, 84 x 52, and 41 x 32, respectively. To resolve high gradients near walls the grid lines were clustered near walls. A laminar flow computation for a 1.54 inch nozzle indicated a constant wall pressure level of about five in the inlet and combustor sections. A Mach number contour plot showed supersonic core flow along the axis. Separated primary and secondary flows were noticed inside the inlet and combustor. A shock reflection pattern consisting of four normal shocks at the axis was observed. A detailed discussion of the separated inlet flow of the present computations can be found in Reference 12. For the laminar flow computation, the computed wall pressure in the inlet section was in fair agreement with data. However, the computed wall pressure for the laminar flow did not match the wind tunnel data in the combustor section. This case, with a nozzle throat diameter of 1.54 inches, was found to be highly sensitive to small changes in model throat diameter. This case is thought to be sensitive due to the following three conditions: (1) separated flow inside the combustor; (2) boundary layer displacement thickness at the nozzle throat; and (3) internal shock reflection pattern. A less than satisfactory prediction of these conditions was thought to be a potential reason for the discrepancy between computed and measured data in the combustor. As shown in Figure 20, this highly sensitive behavior is visible in experimental measurements for three different wind tunnel runs

for nozzle throat diameters of 1.54 inches and 1.534 inches (Reference 13). In an attempt to simulate the separated flow, a modified Baldwin-Lomax turbulence model[14] was incorporated in the code. The computed wall pressure with this turbulence model showed a trend that is similar to one that was observed experimentally inside the combustor (Figure 20). Although, this modified model seems to help for this particular case, critical evaluation based on separated flow test cases will be required before making any specific conclusion about the model. A plot of Mach number contours (Figure 21) shows a series of shock reflections which coalesce into a normal shock in the middle of the combustor. The flow between this shock and the nozzle throat is essentially subsonic. A normalized pressure contour plot for the same case is shown in Figure 22. To obtain a normal shock at the lip of the inlet, a series of computations were made with gradual reduction in the nozzle throat diameter. At a nozzle throat diameter of 1.21 inches, a normal shock at the lip of the inlet was observed (Figure 23). The computed wall pressure level shown in Figure 24, is in fair agreement with wind tunnel data (not shown) for a nozzle throat diameter of 1.25 inches as shown in Figure 24, see Reference 10.

CONCLUDING REMARKS

A computer code has been developed that incorporates a zonal grid technique to handle complex flow configurations and a parallel algorithm to exploit new multiprocessor architectures. The code has been exercised on the Intel IPSC hypercube and CRAY X-MP/48 computers to verify the ability to perform parallel computations for realistic fluid dynamic problems.

The results of several test cases which demonstrated the ability of the zonal technique to compute highly complex flow cases have been discussed.

It is felt that the parallel programming techniques are working very well and that the code has excellent potential for performing computations for complex configurations such as guided and non axisymmetric projectiles. Further development of the code is continuing with emphasis placed on extensions to three-dimensions and multi-tasking on the CRAY X-MP/48.
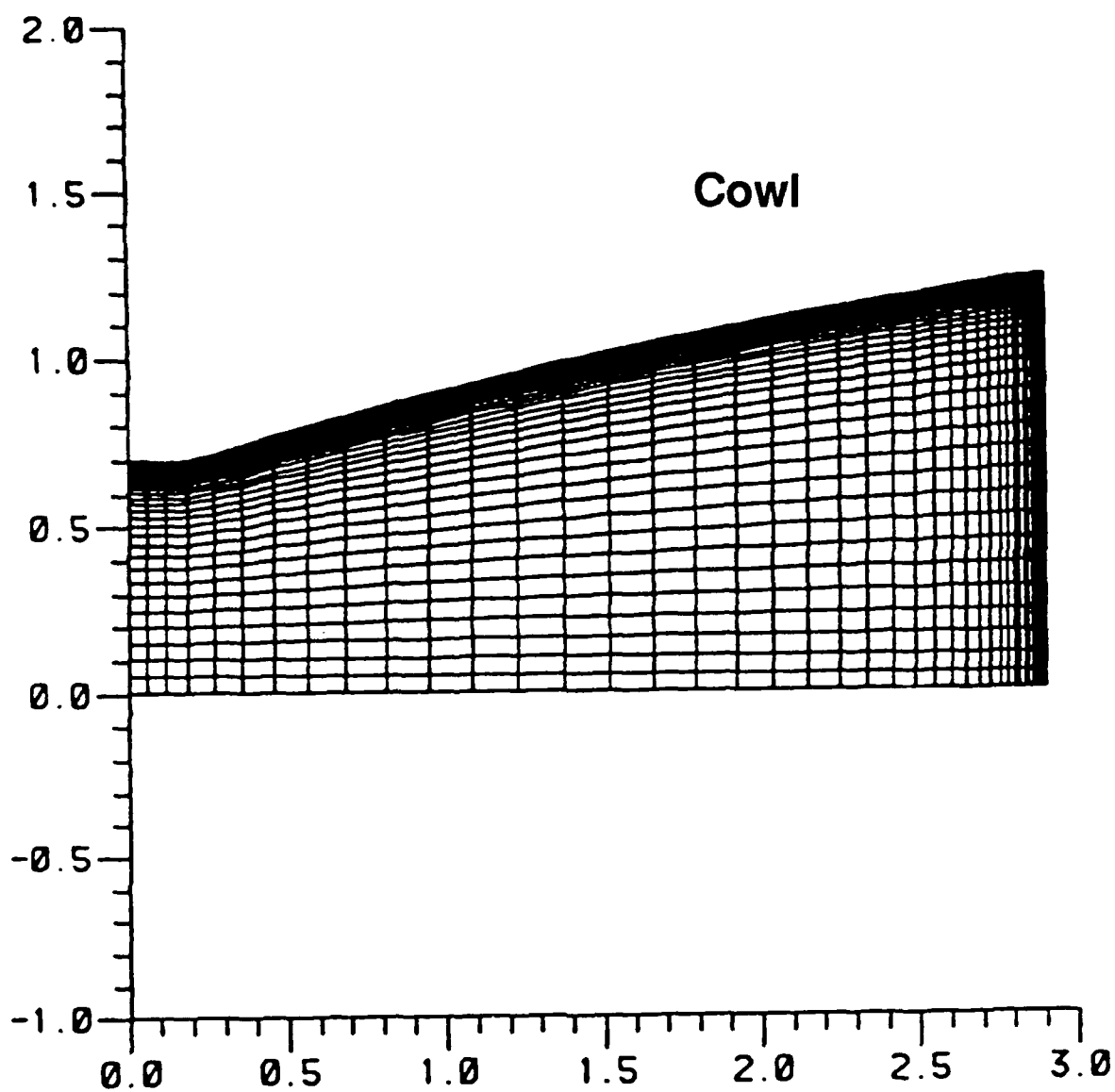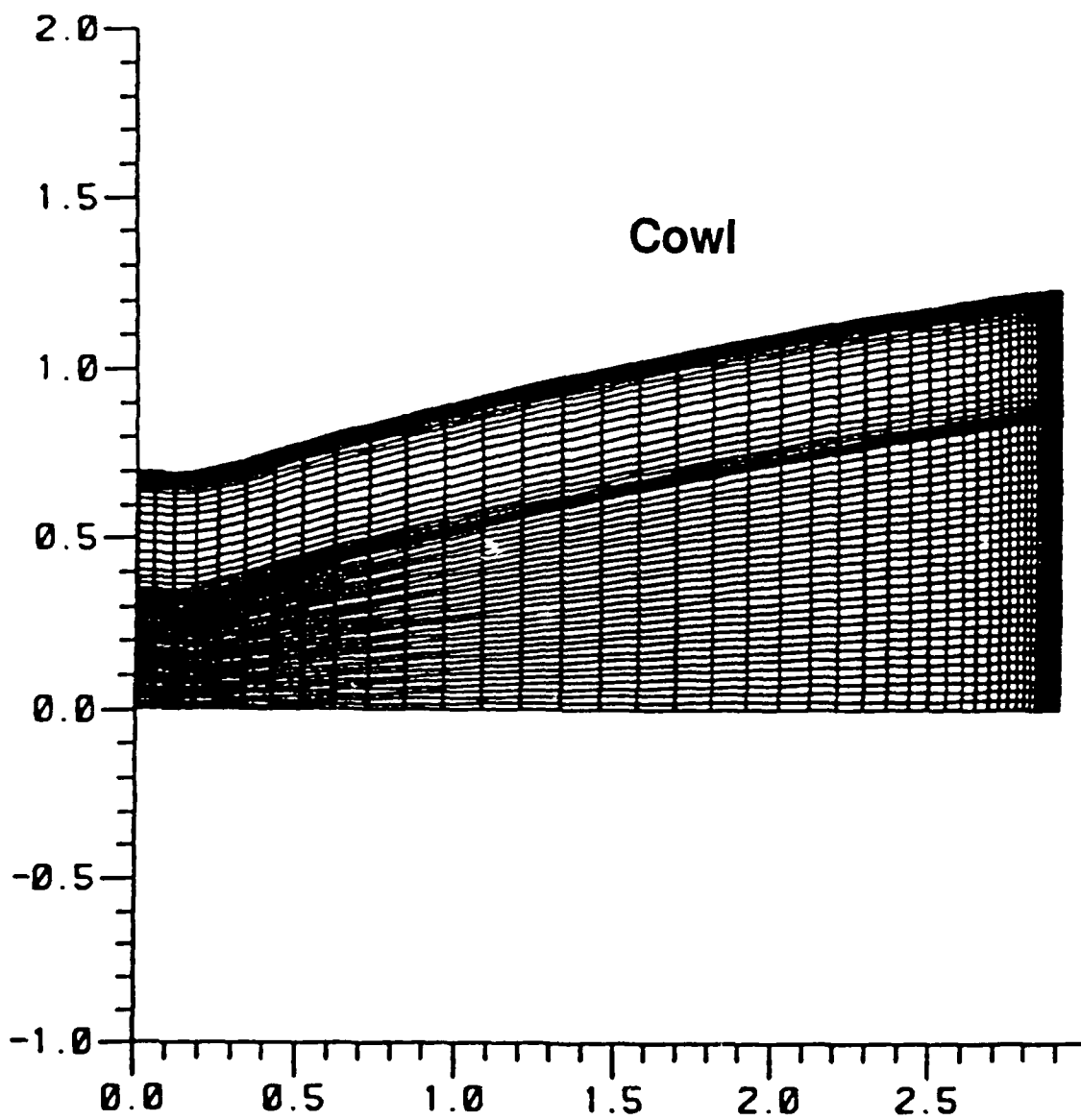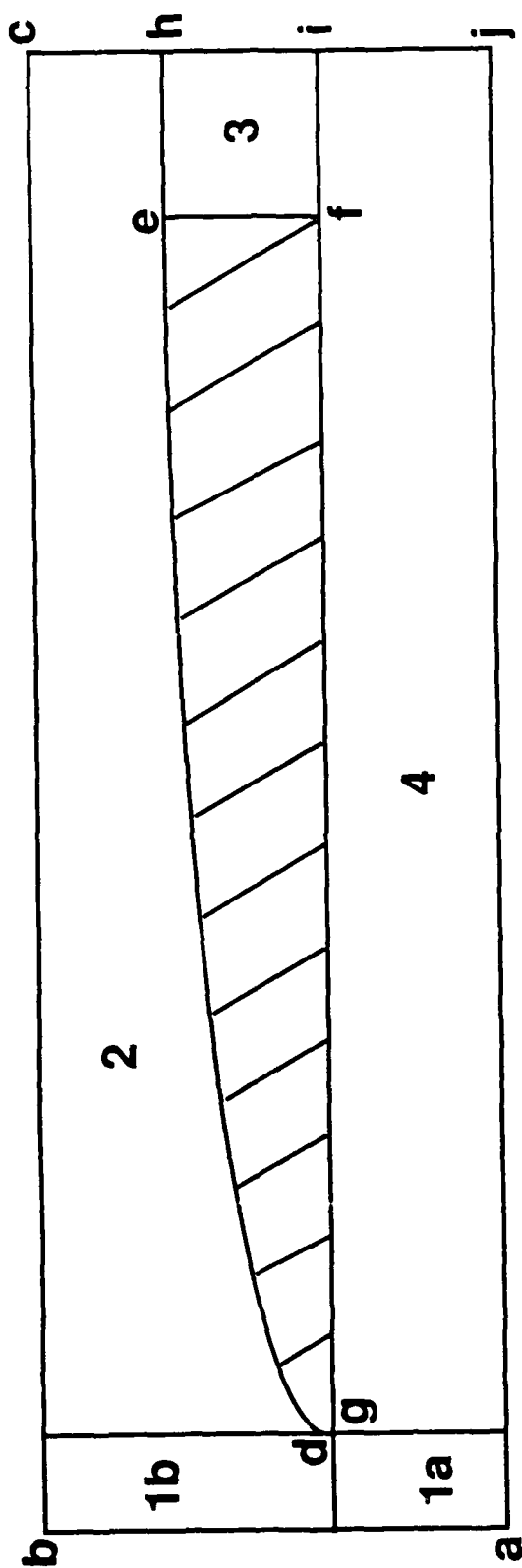
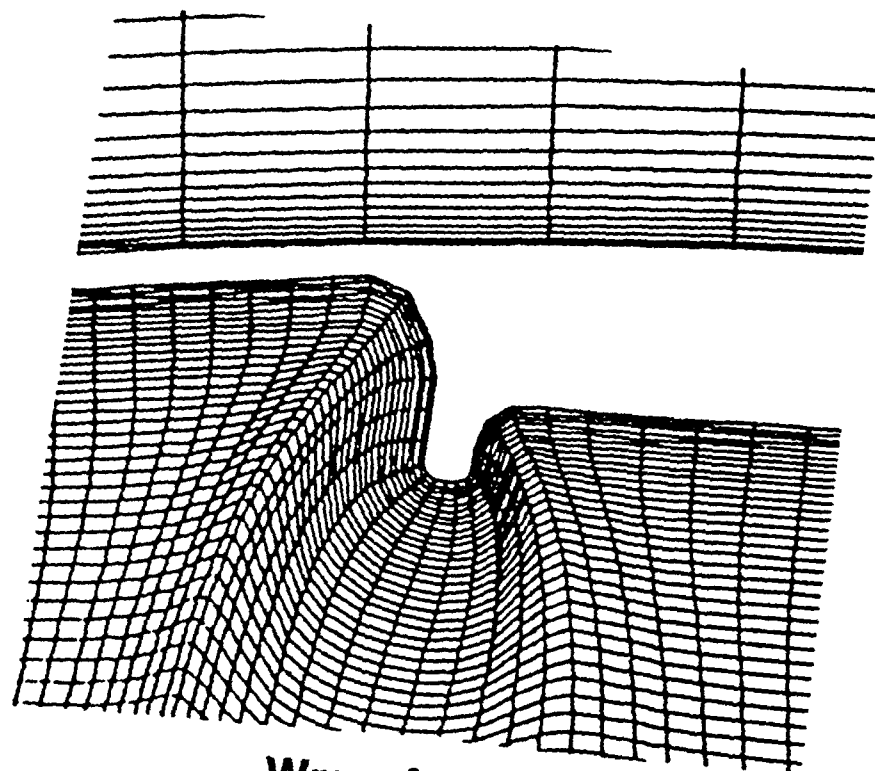Figure 1. Fully clustered grid for cowl region

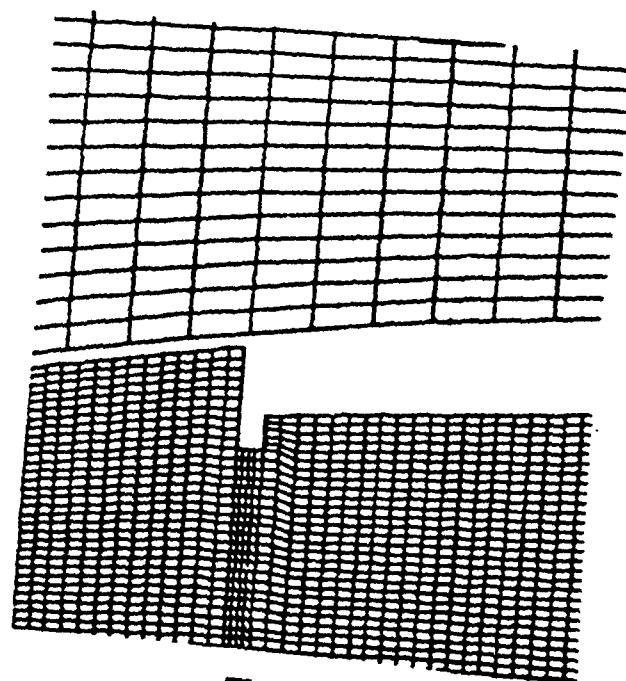Figure 2. Partly clustered partly uniform grid for cowl region

Figure 3. Zonal boundary conditions

ab - Freestream
bc - No Reflection
defg - Wall, No Slip

aj - Symmetry
chij - Outflow

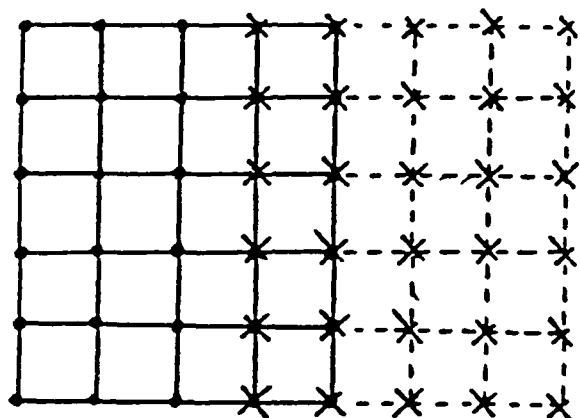19

Wrap Around

Zonal

Figure 4. Grids at the intersection of cowl and injector

● SUBDOMAIN A   ✗ SUBDOMAIN B

Figure 5. One grid-cell overlap
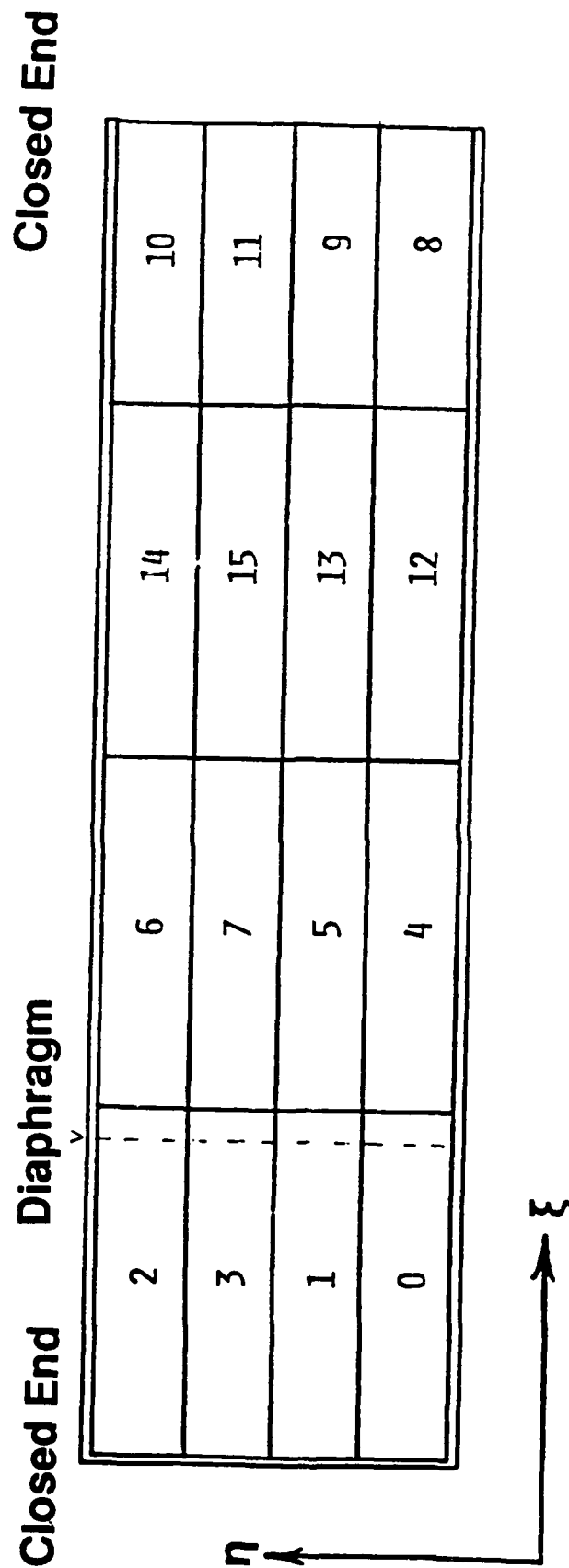
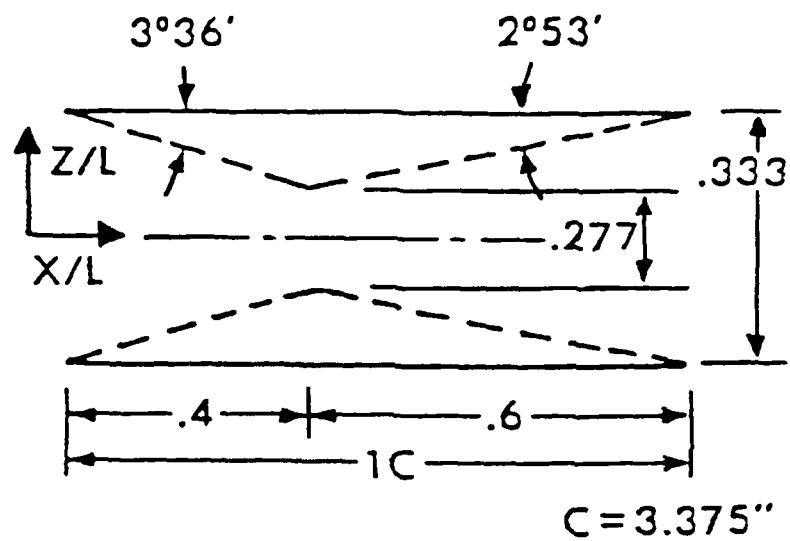Figure 6. Sixteen computational subdomains for a constant area shock tube
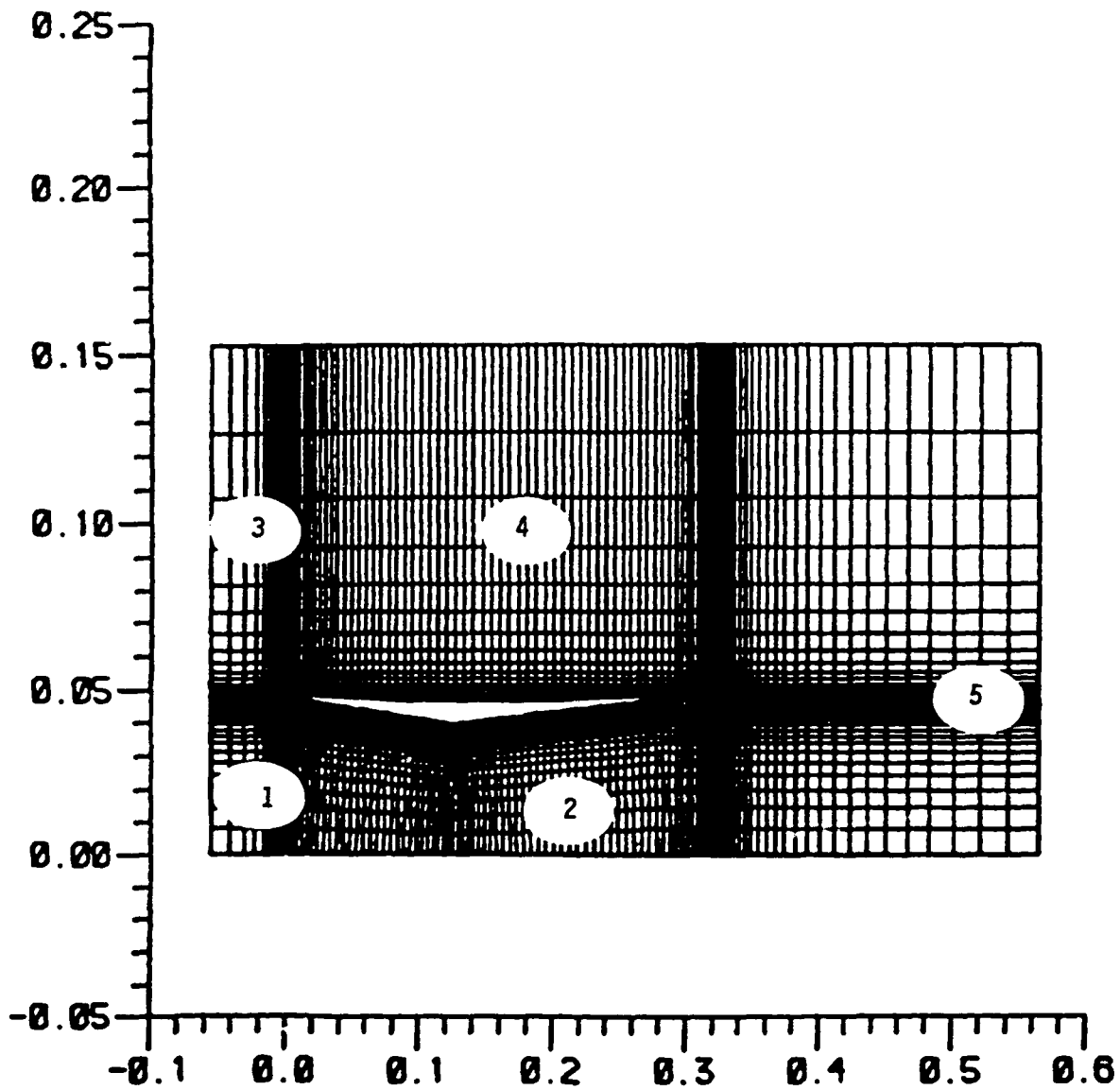
Figure 7. Experimental supersonic tubular projectile model

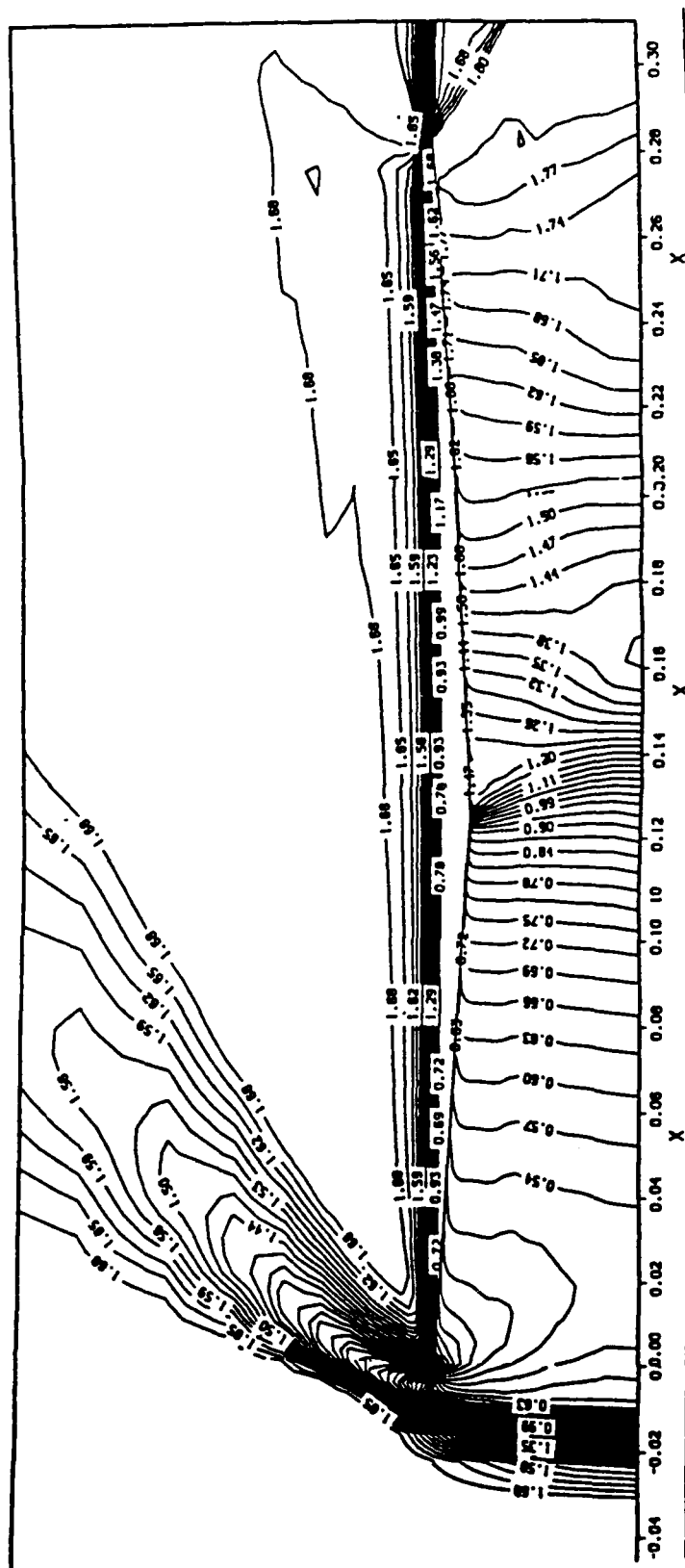Figure 8. A five-zone grid for the tubular projectile

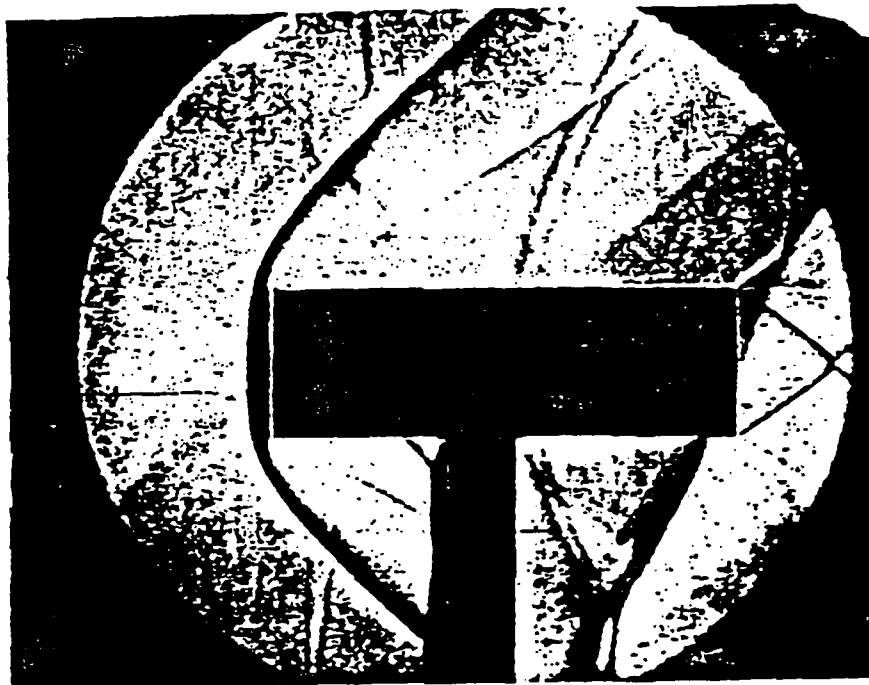Figure 9a. Mach number contours for the tubular projectile, $M_\infty = 1.7$ (Inviscid)

Figure 9b. Mach number contours for the tubular projectile, M_∞ = 1.7 (Viscous)

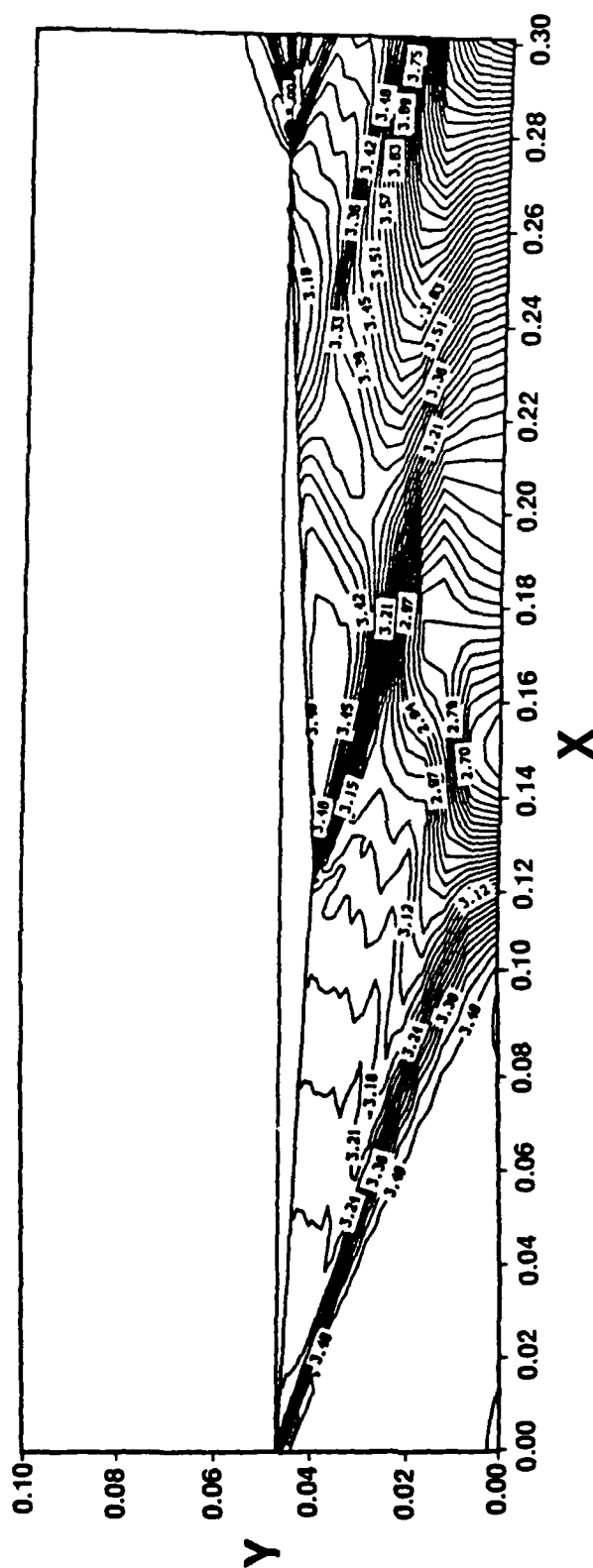Figure 10. Wind tunnel Schlieren photograph, $M_\infty = 1.7$

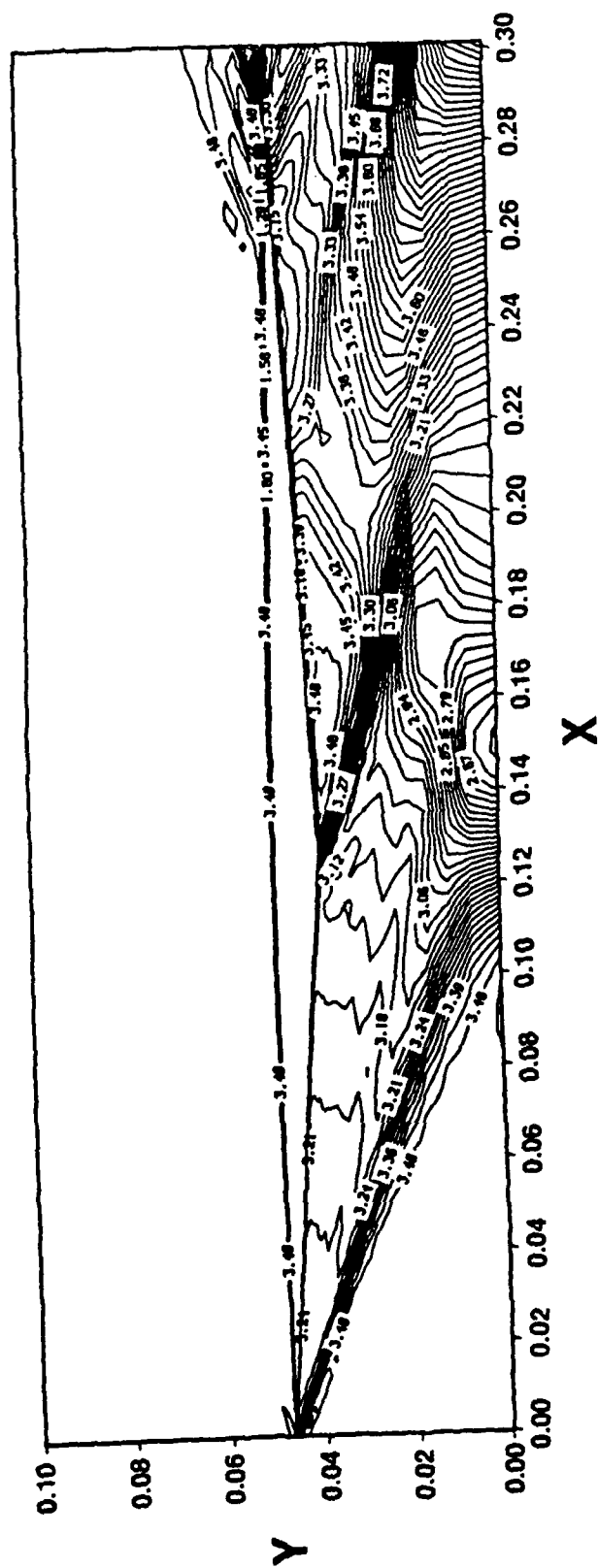Figure 11.   Mach number contours for the tubular projectile, $M_\infty = 3.5$ (Inviscid)

Figure 12. Mach number contours for the tubular projectile, M_∞ = 3.5 (Viscous)
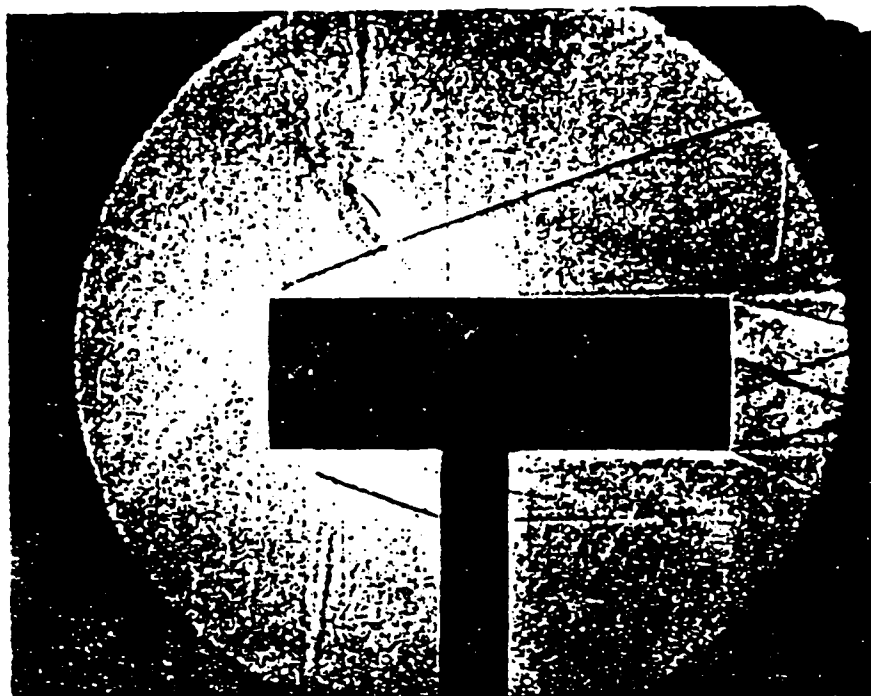
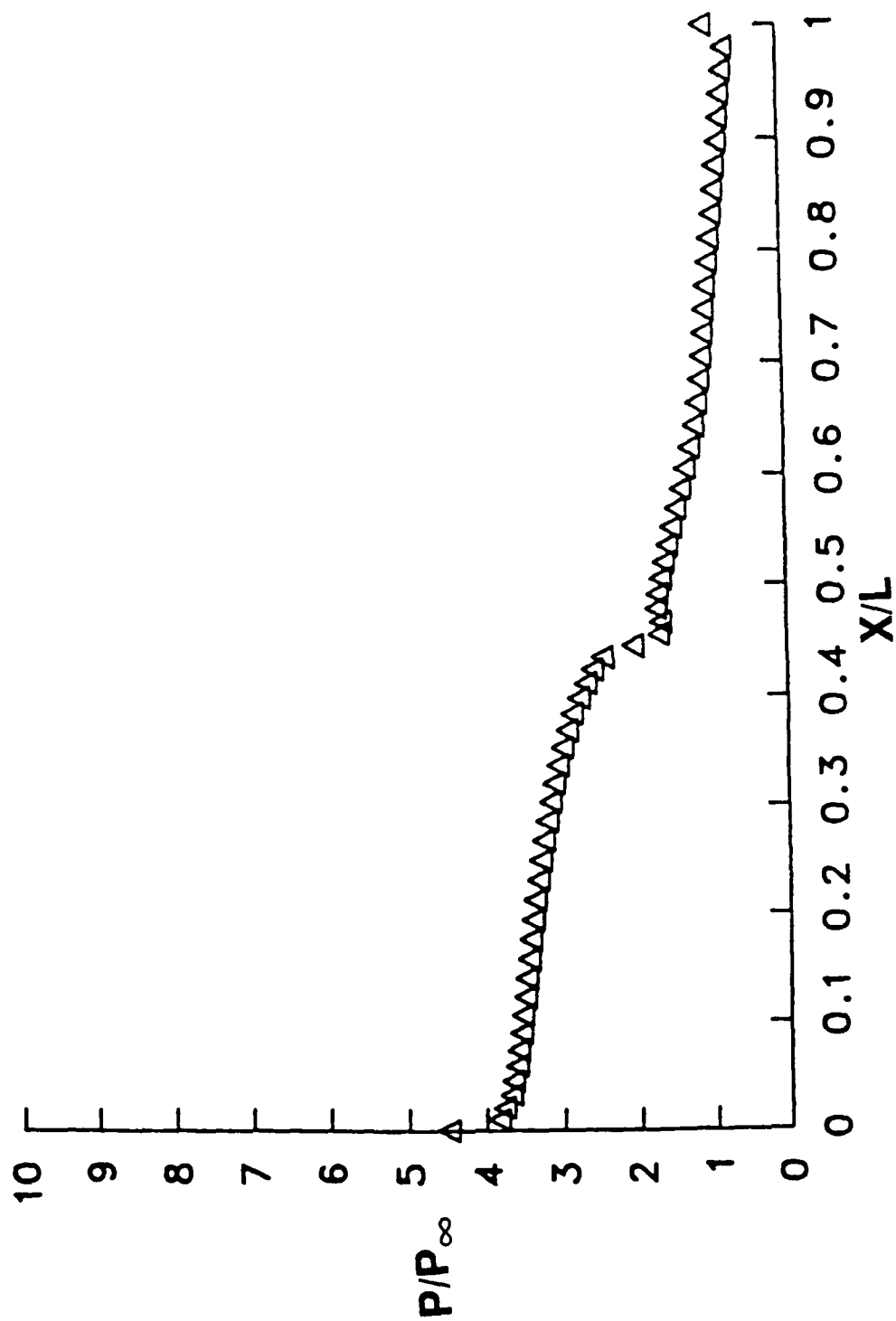Figure 13. Wind tunnel Schlieren photograph, $M_\infty = 3.5$

Figure 14. Internal surface pressure distribution for the tubular projectile, $M_\infty = 1.7$
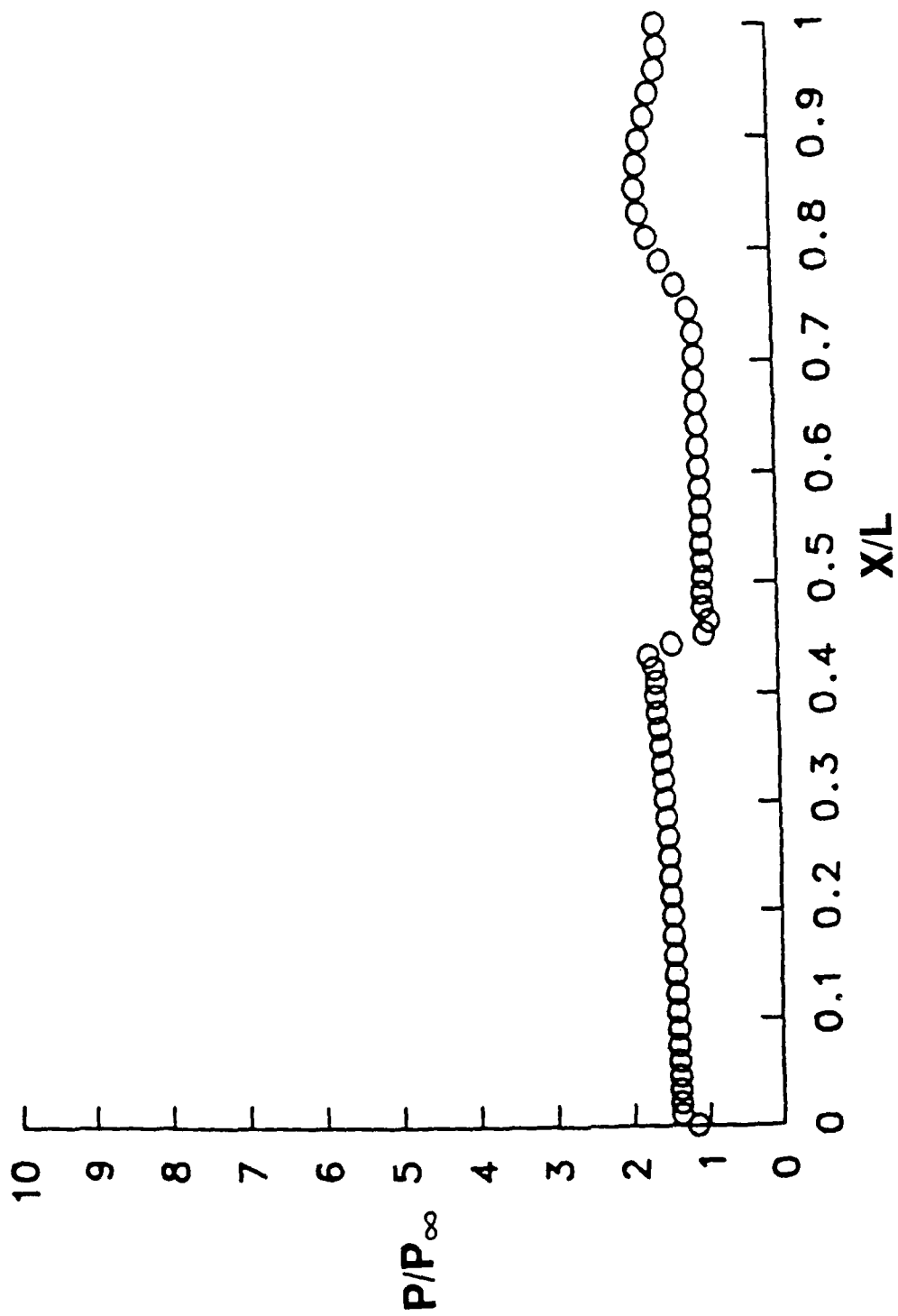
Figure 15. Internal surface pressure distribution for the tubular projectile, $M_\infty = 3.5$

Figure 16a. Schematic illustration of ramjet and boundary conditions

ab – freestream   da – symmetric
bc – no reflection   efge – wall
cd – downstream
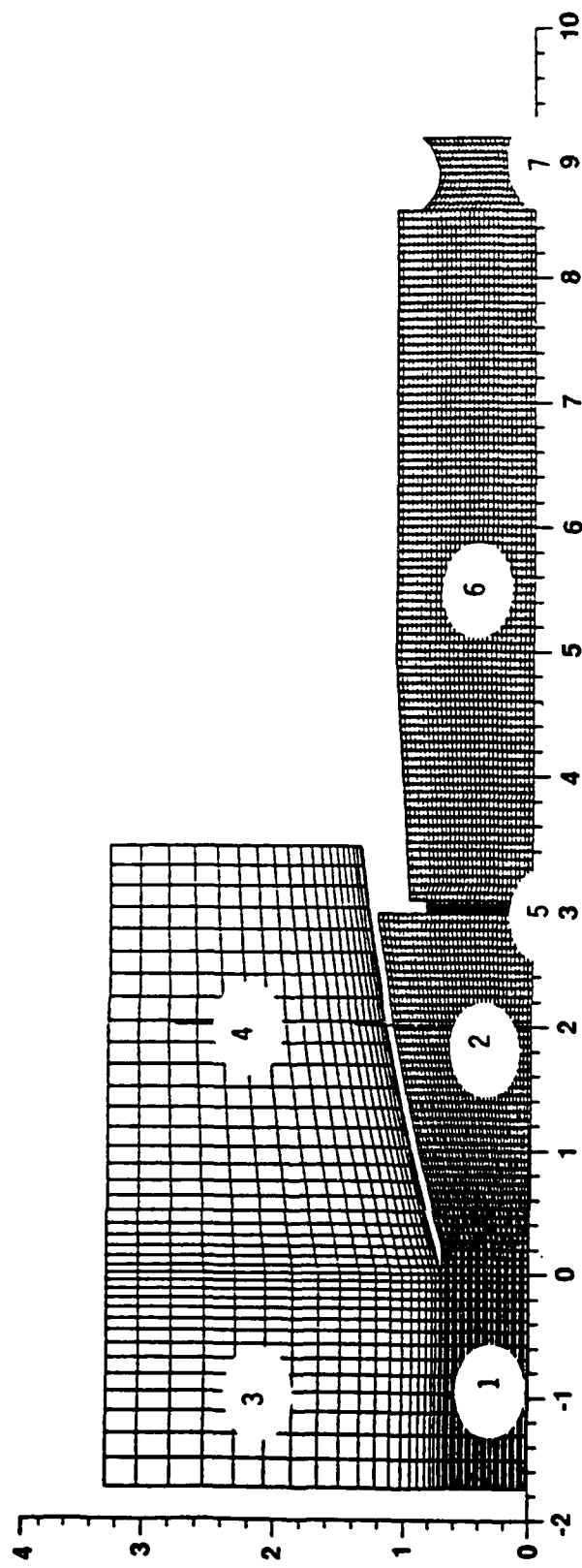
Figure 16b. Seven-zone grid for the ramjet
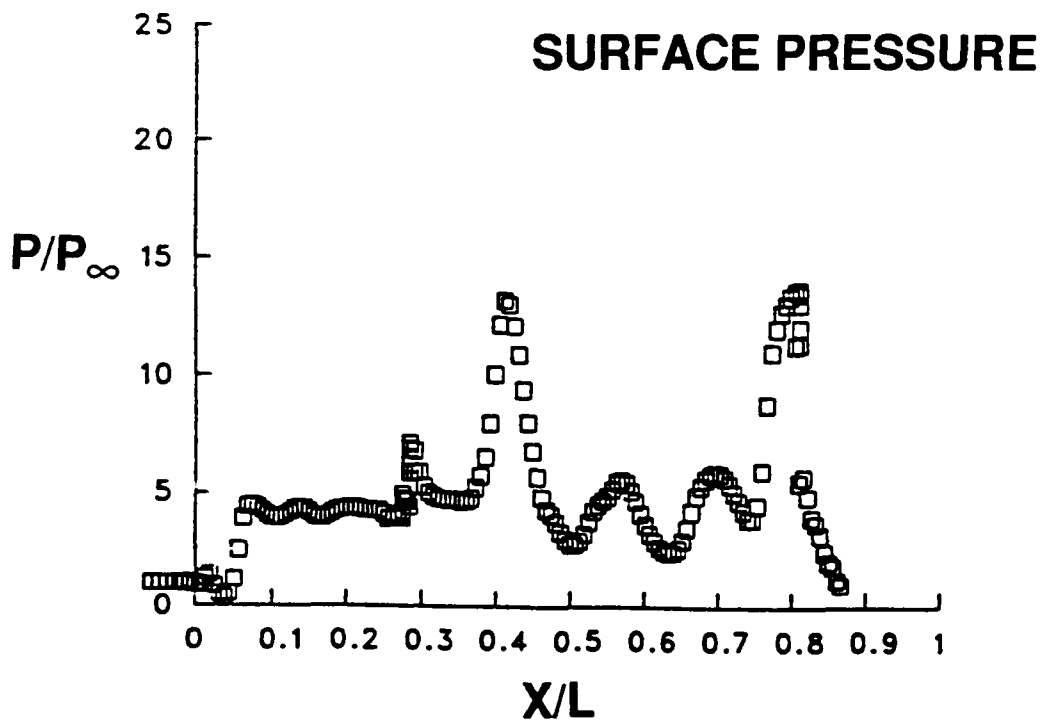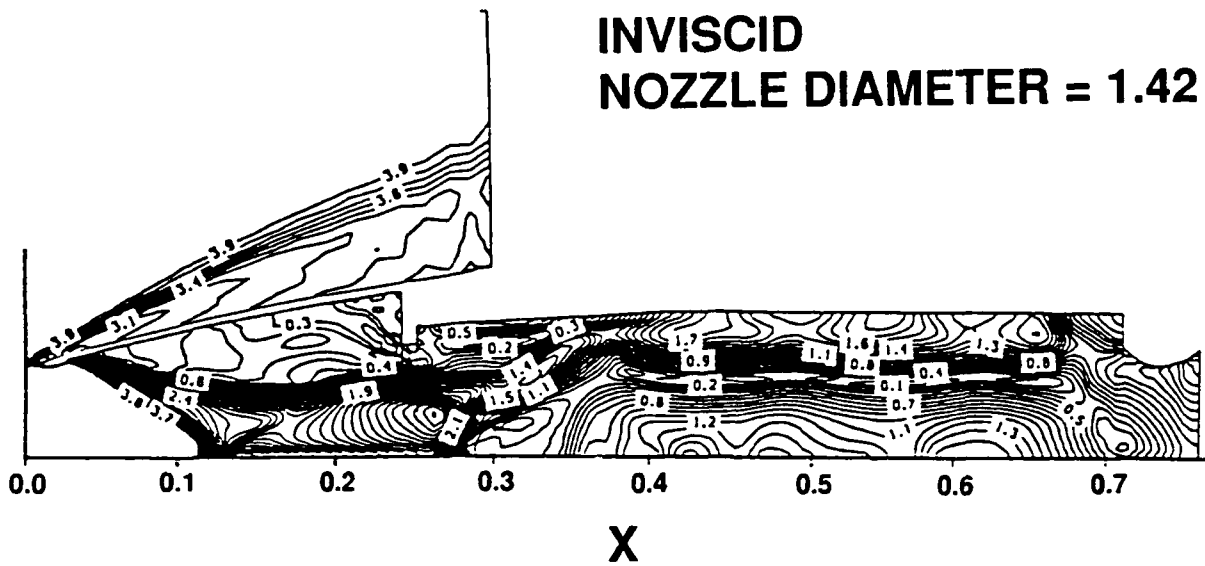
Figure 17. Mach number contours and internal surface pressure distribution
for the ramjet with nozzle throat diameter of 1.42
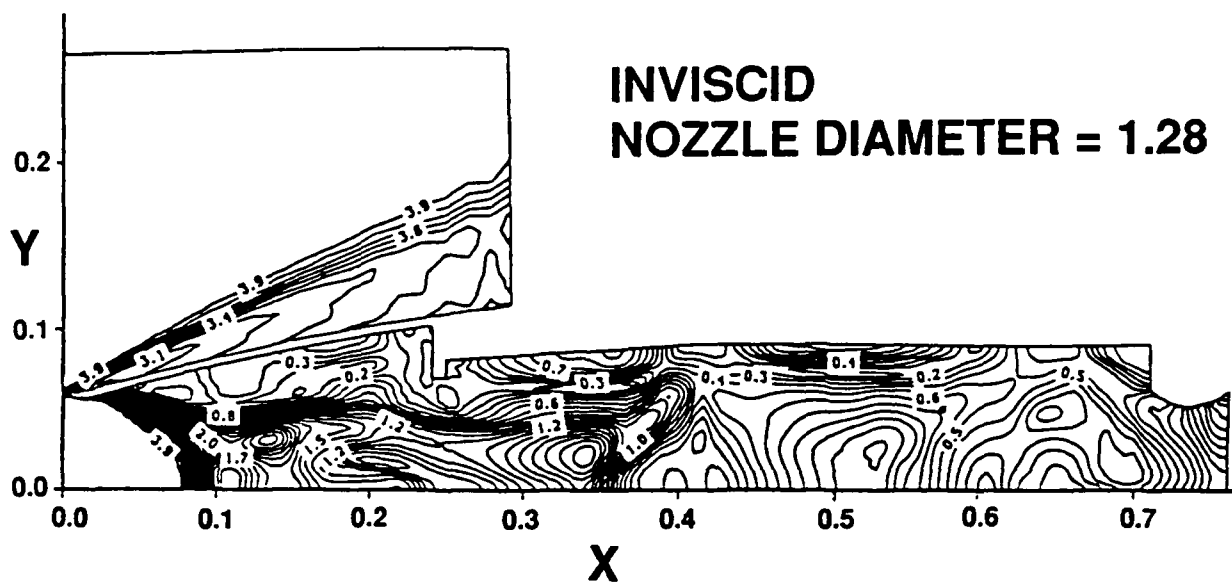
Figure 18a. Mach number contours showing a strong oblique shock in the inlet region
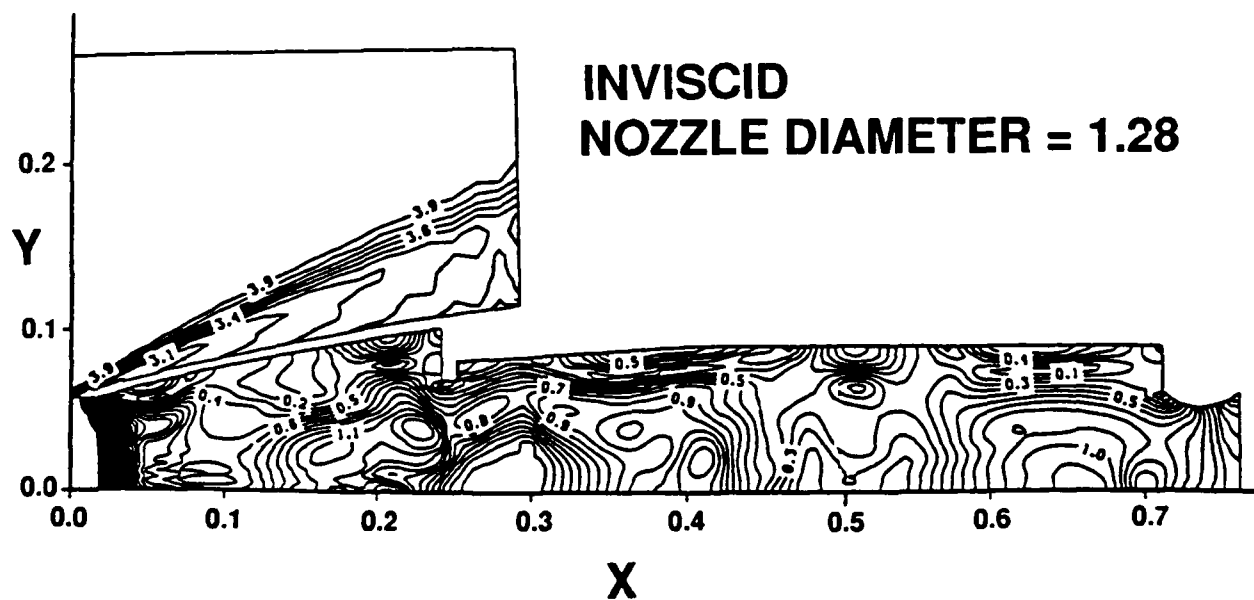
Figure 18b. Mach number contours showing a normal shock in the inlet region

INVISCID
NOZZLE DIAMETER = 1.28
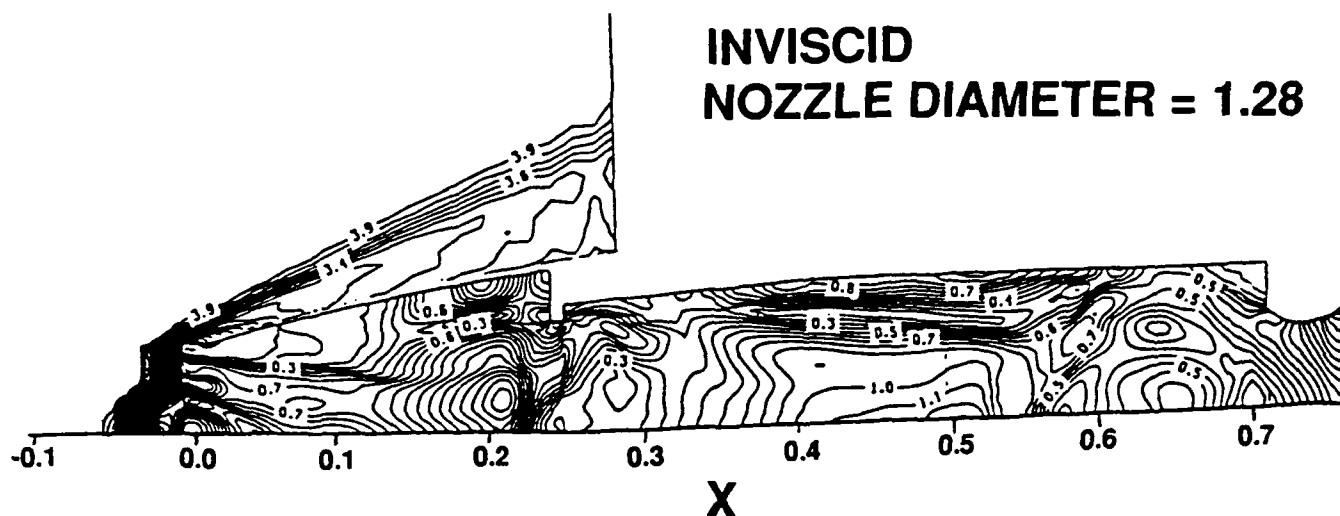
Figure 18c. Mach number contours showing an attached normal shock at the cowl lip

INVISCID
NOZZLE DIAMETER = 1.28
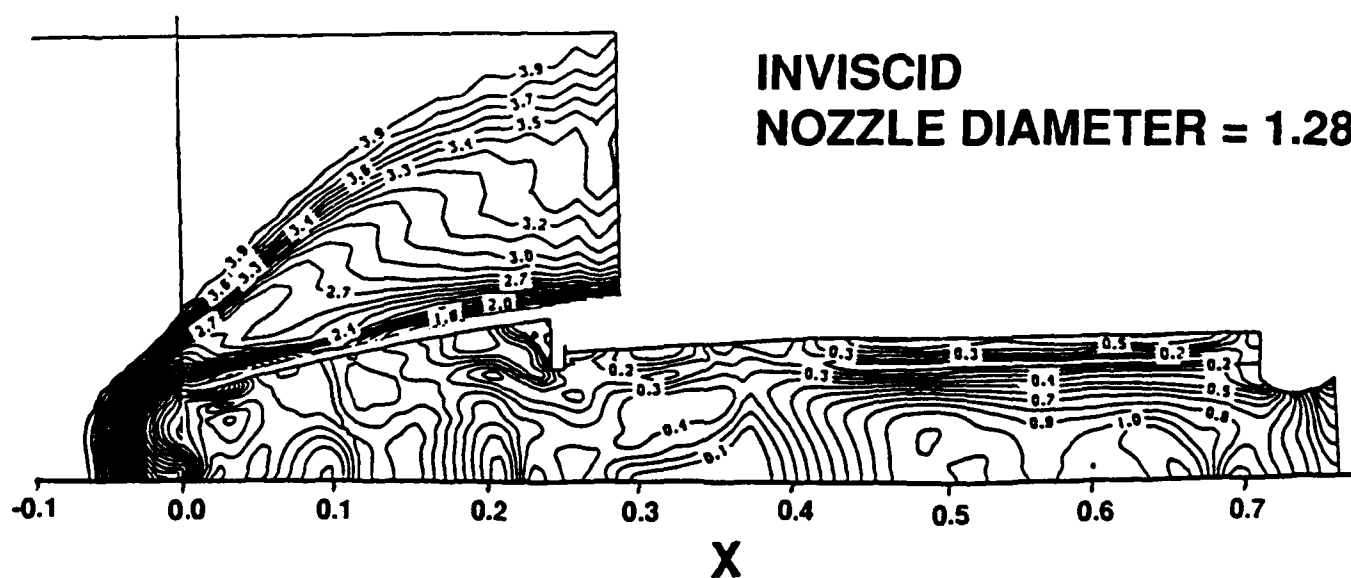
Figure 18d. Mach number contours showing a detached bow shock
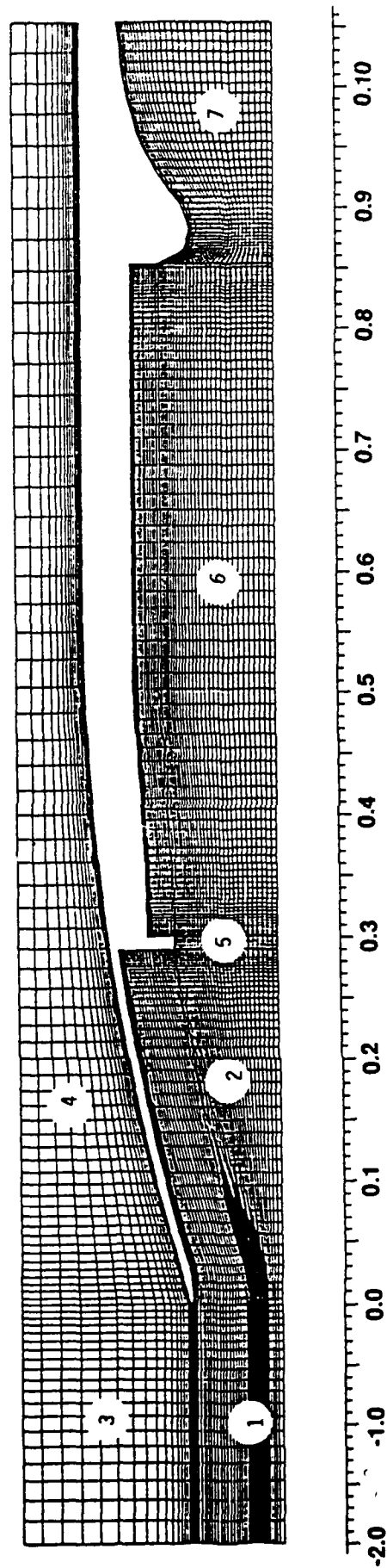
Figure 19. Grid for viscous computation
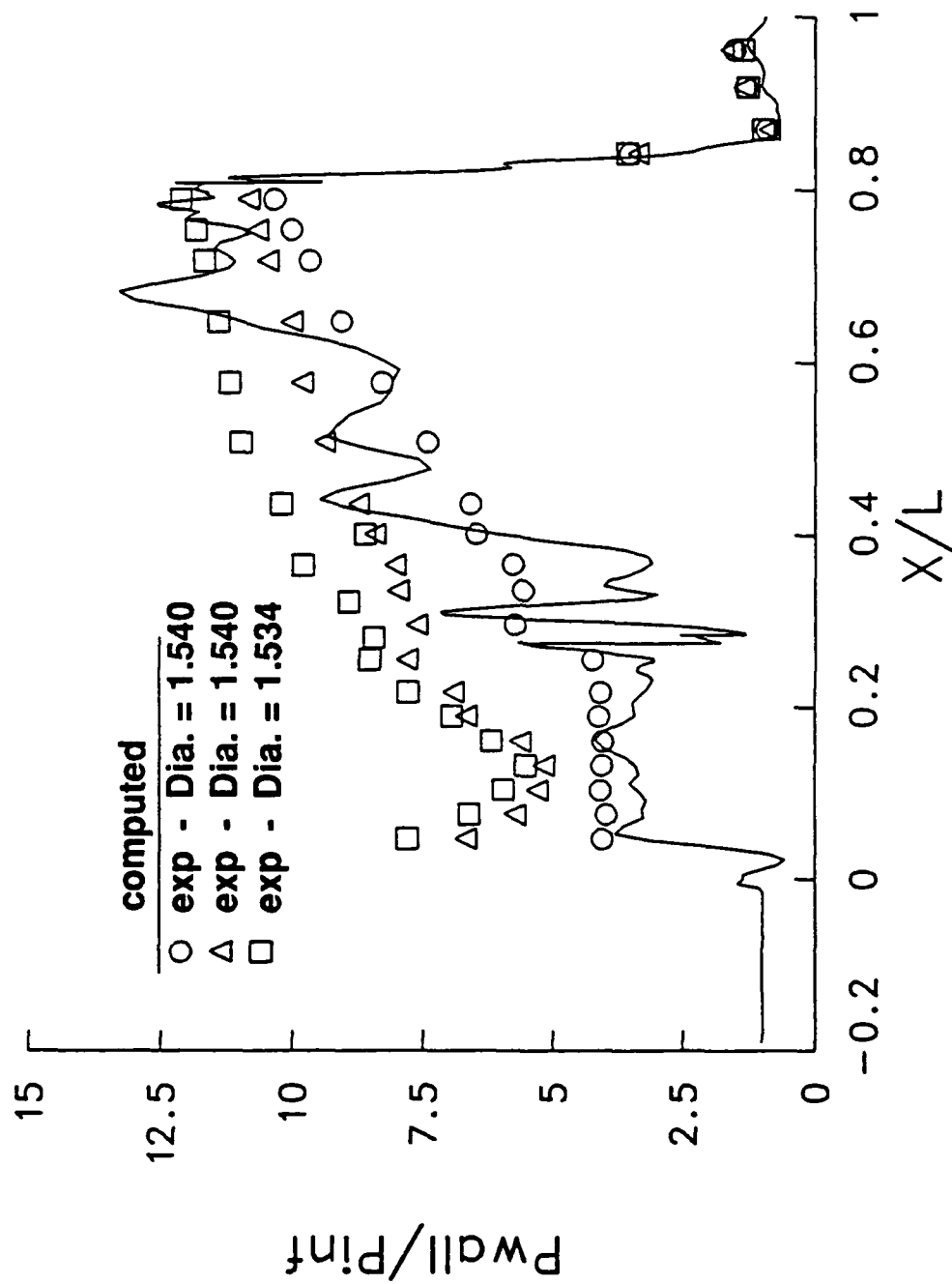
Figure 20. Internal surface pressure distribution for the ramjet with 1.54 inch nozzle diameter
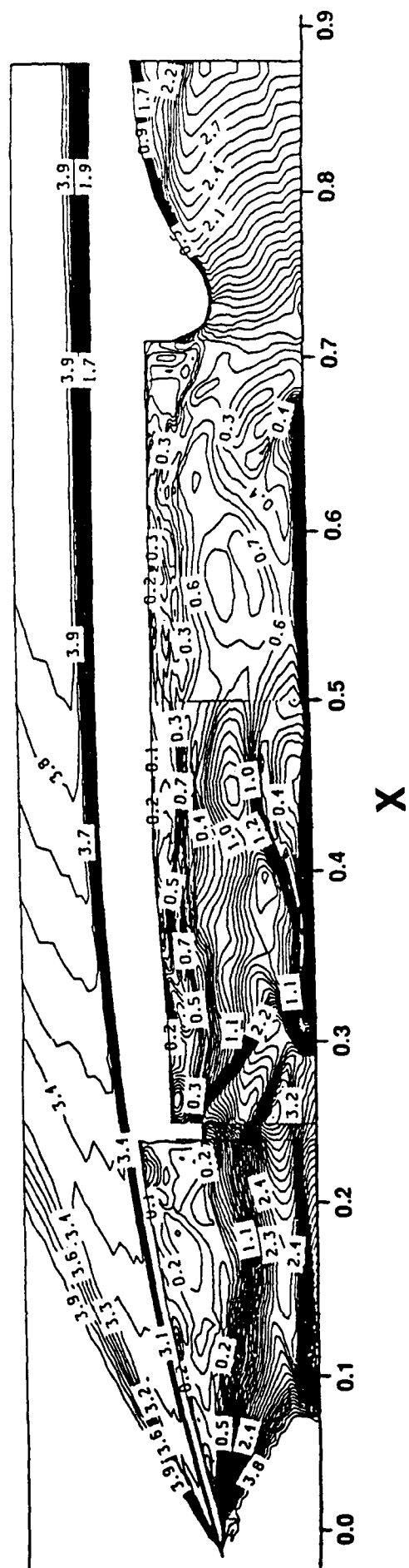
Figure 21. Mach number contours for the ramjet with 1.54 inch nozzle diameter

Figure 22. Normalized pressure contours for the ramjet with 1.54 inch nozzle diameter

41
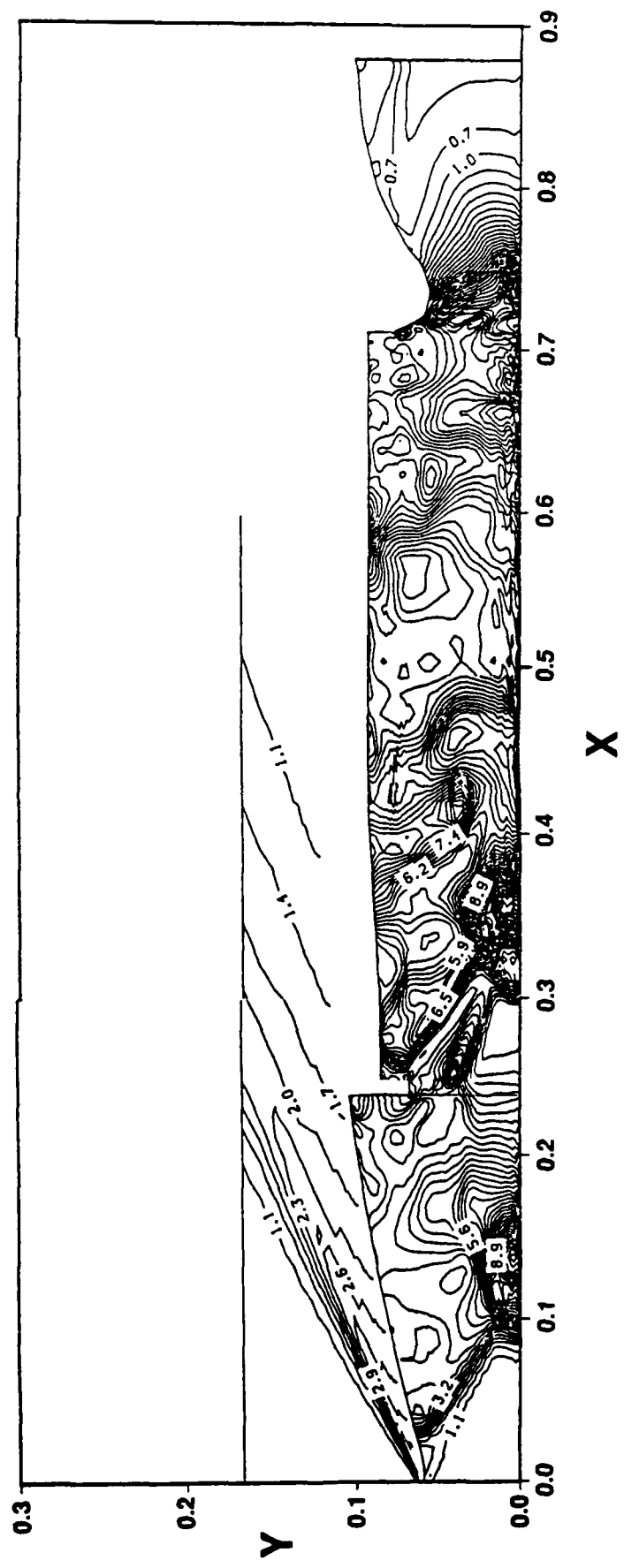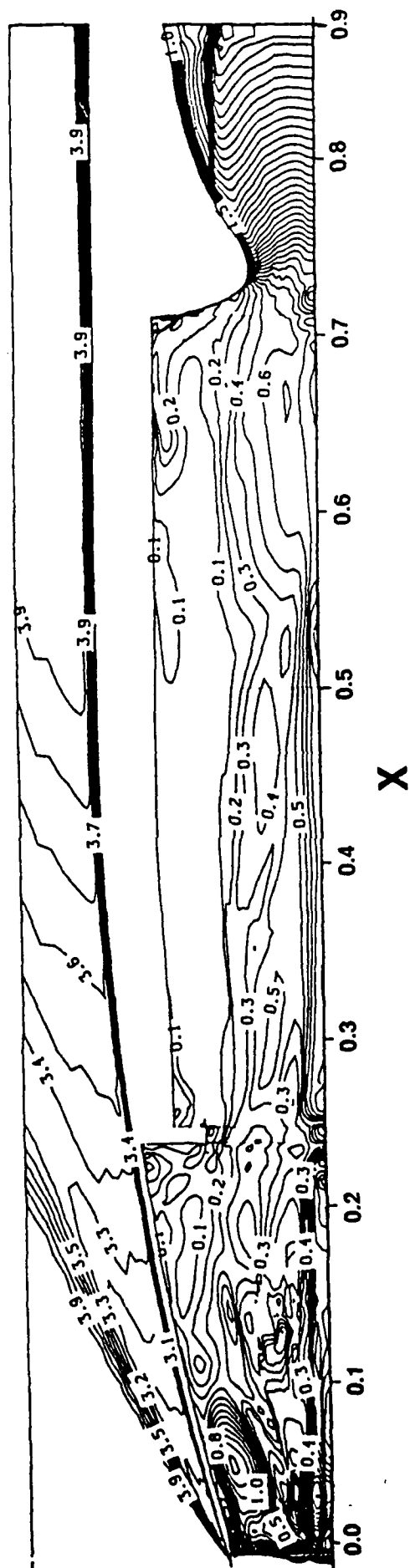
Figure 23. Mach number contours for the ramjet with 1.21 inch nozzle diameter
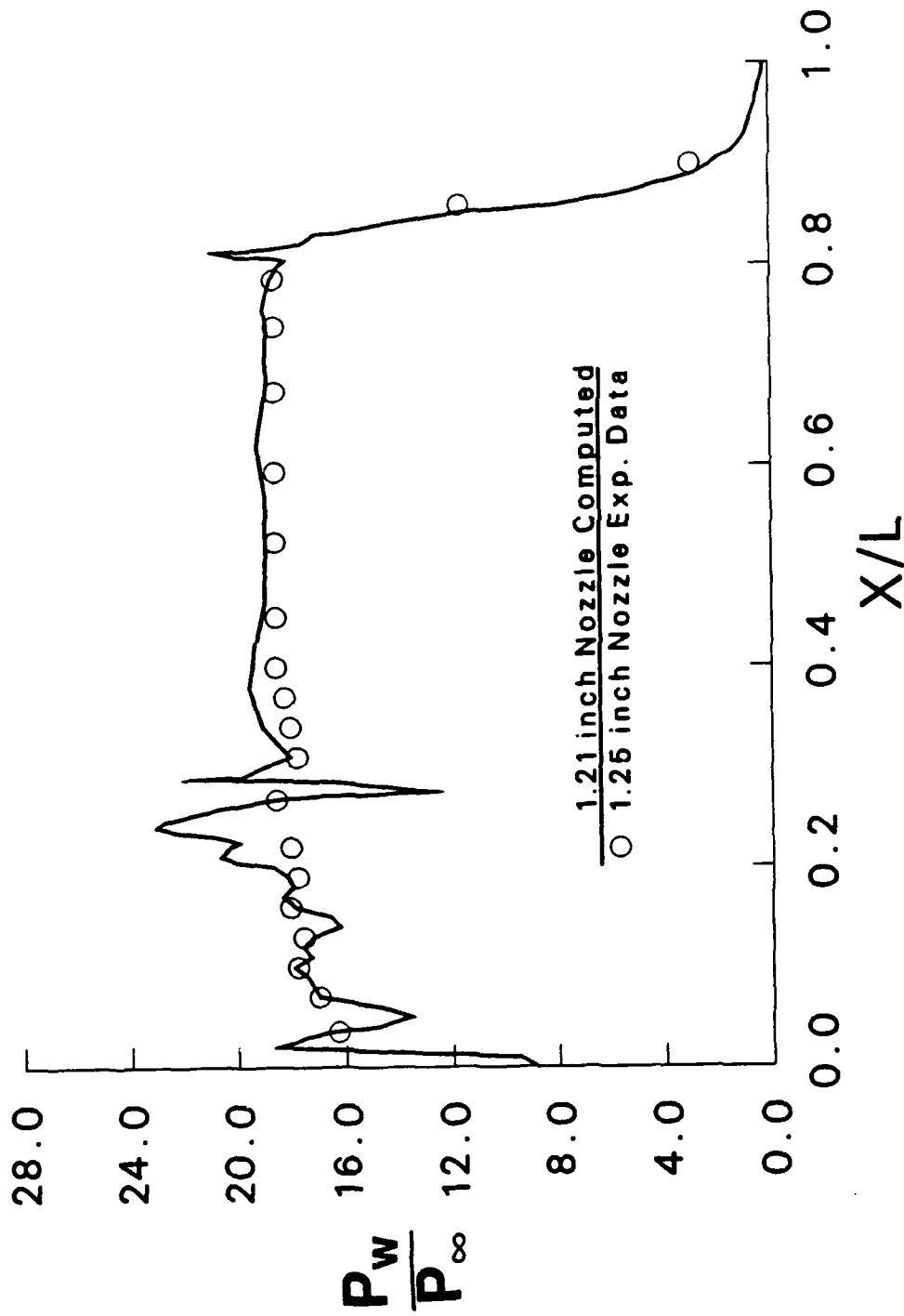
Figure 24. Internal surface pressure distribution for the ramjet with 1.21 inch nozzle diameter

(THIS PAGE WAS INTENTIONALLY LEFT BLANK)

REFERENCES

1. Vinokur, Marcel, "On One-Dimensional Stretching Functions for Finite-Difference Calculations," NASA CR 3313, Ames Research Center, 1980.

2. MacCormack, R.W., "The Effects of Viscosity in Hypervelocity Impact Cratering," AIAA Paper No. 69-354, 1969.

3. MacCormack, R.W. and Baldwin, B.S., "A Numerical Method for Solving the Navier-Stokes Equations with Application to Shock-Boundary Layer Interactions," AIAA Paper No. 75-1, 1975.

4. MacCormack, R.W., "Numerical Solution of the Interaction of a Shock Wave with a Laminar Boundary Layer," Lecture Notes in Physics, Vol. 8, 1972.

5. Rai, M.M., "A Conservative Treatment of Zonal Boundaries for Euler Equation Calculations," AIAA Paper No. 84-0164, 1984.

6. Benek, J.A., Steger, J.L. and Dougherty, F.C., "A Flexible Grid Embedding Technique with Application to the Euler Equations," AIAA Paper No. 83-1944, 1983.

7. Berger, M.J., "On Conservation at Grid Interfaces," ICASE Report No. 84-43, 1984.

8. Lombard, C.K. and Venkatapathy, E., "Implicit Boundary Treatment for Joined and Disjoint Patched Mesh Systems," AIAA Paper No. 85-1503, 1985.

9. Misegades, K.P., Private communication concerning microtasking on the CRAY X-MP/48, CRAY Research, Inc., Mendota Heights, MN.

10. Kayser, L.D., Yalamanchili, R.J., and Trexler, C.A., "Pressure Measurements on the Interior Surface of a 75mm Tubular Projectile at Mach 4," US Army Ballistic Research Laboratory, Aberdeen Proving Ground, Maryland, BRL-MR-3725, December 1988.

11. Oskay, V., Private communication concerning aerodynamic range tests of the 20mm SFRJ, BRL, Aberdeen Proving Ground, MD

12. Danberg, J.E. and Sigal, A., "Evaluation of Solid Fuel Ramjet Projectile Aerodynamics Characteristics," Proceedings of the 8th ADPA International Symposium on Ballistics, San Diego, CA, October 1987.

13. Yalamanchili, R.J., Private communication concerning wind tunnel measurements of the 75mm SFRJ, BRL, Aberdeen Proving Ground, MD.

14. Danberg, J.E. and Patel, N.R., "An Algebraic Turbulence Model for Flow Separation Caused by Forward and Backward Facing Steps," US Army Ballistic Research Laboratory, Aberdeen Proving Ground, Maryland, BRL-MR-3791, December 1989.

(THIS PAGE WAS INTENTIONALLY LEFT BLANK)

LIST OF SYMBOLS

B_i	coefficient in Navier-Stokes equation
C_j	coefficient in Navier-Stokes equation
c	speed of sound
C_p	specific heat at constant pressure
C_v	specific heat at constant volume
D_i	coefficient in Navier-Stokes equation
E	flux vector in ξ direction
e	total energy per unit mass
F	flux vector in η direction
G_1, G_2	vectors of axisymmetric viscous terms
H	source term in Navier-Stokes equation
J	Jacobian of coordinate transformation
M	Mach number
Pr	molecular Prandtl number
Pr_t	turbulent Prandtl number
P	static pressure
Q	vector of dependent variables
R·	gas constant
S_1, S_2	vectors of viscous terms
T	static temperature
T_1, T_2	vectors of viscous terms
t	time
u,v	Cartesian velocity components
U,V	contravariant velocity components
x,y	physical Cartesian coordinates
α	pressure damping coefficient

μ	molecular dynamic viscosity
ε	turbulent eddy viscosity
ξ, η	transformed coordinates
ρ	density

Subscripts

i,j	mesh indices
∞	free stream condition

APPENDIX A: NON-REFLECTING OUTER BOUNDARY CONDITION

This appendix describes the derivation of the nonreflecting outer boundary condition employed along the top boundary (Figure 3). The non-reflection boundary condition, like many other Neumann type boundary conditions, is an approximation. For appropriate supersonic flow applications, the use of non-reflection boundary conditions allows the outer boundary to be placed close to the body. This substantially reduces the number of grid points required for a given application and reduces both computer storage and CPU time requirements. This boundary condition is consistent when the following conditions are met.

a. The local Mach number is greater than one at the boundary.

b. There is a family of outward running Mach lines.

Consider a nonorthogonal coordinate system as shown in Figure A1. Through point x,y one can draw the velocity vector and Mach wave inclined at an angle μ with respect to the velocity vector. The velocity vector is at an angle measured with respect to Cartesian coordinate x. This gives

$$\mu = \sin^{-1} \frac{1}{M}$$

and

$$\omega = \tan^{-1} \frac{v}{u}$$

which leads to a total included angle

$$\theta = \mu + \omega$$

let
$$f = f(\rho, u, v, T)^T.$$

The non-reflection condition requires that the flow variables remain constant along the left running Mach lines.

$$f_{i,JL} = f_{x,y}$$

which gives

$$f_{x,y} = f_{k-1, JL-1} + \frac{A}{B(f_{K,JL-1} - f_{k-1,JL-1})}$$

where

$$x = \frac{(y_{k,JL-1} - y_{i,JL} + x_{i,JL} \tan \theta - x_{k,JL-1} \tan \Psi)}{(\tan \theta - \tan \Psi)}$$

49

$$y = y_{i,JL} + \tan \theta \ (x - x_{i,JL})$$

$$\Delta x = x_{k,JL-1} - x_{k-1, JL-1}$$

$$\Delta y = y_{k,JL-1} - y_{k-1, JL-1}$$

$$\Psi = \tan^{-1} \ (\Delta y / \Delta x)$$

$$A = \{(x - x_{k-1, JL-1})^2 + (y - y_{k-1, JL-1})^2\}^{1/2}$$

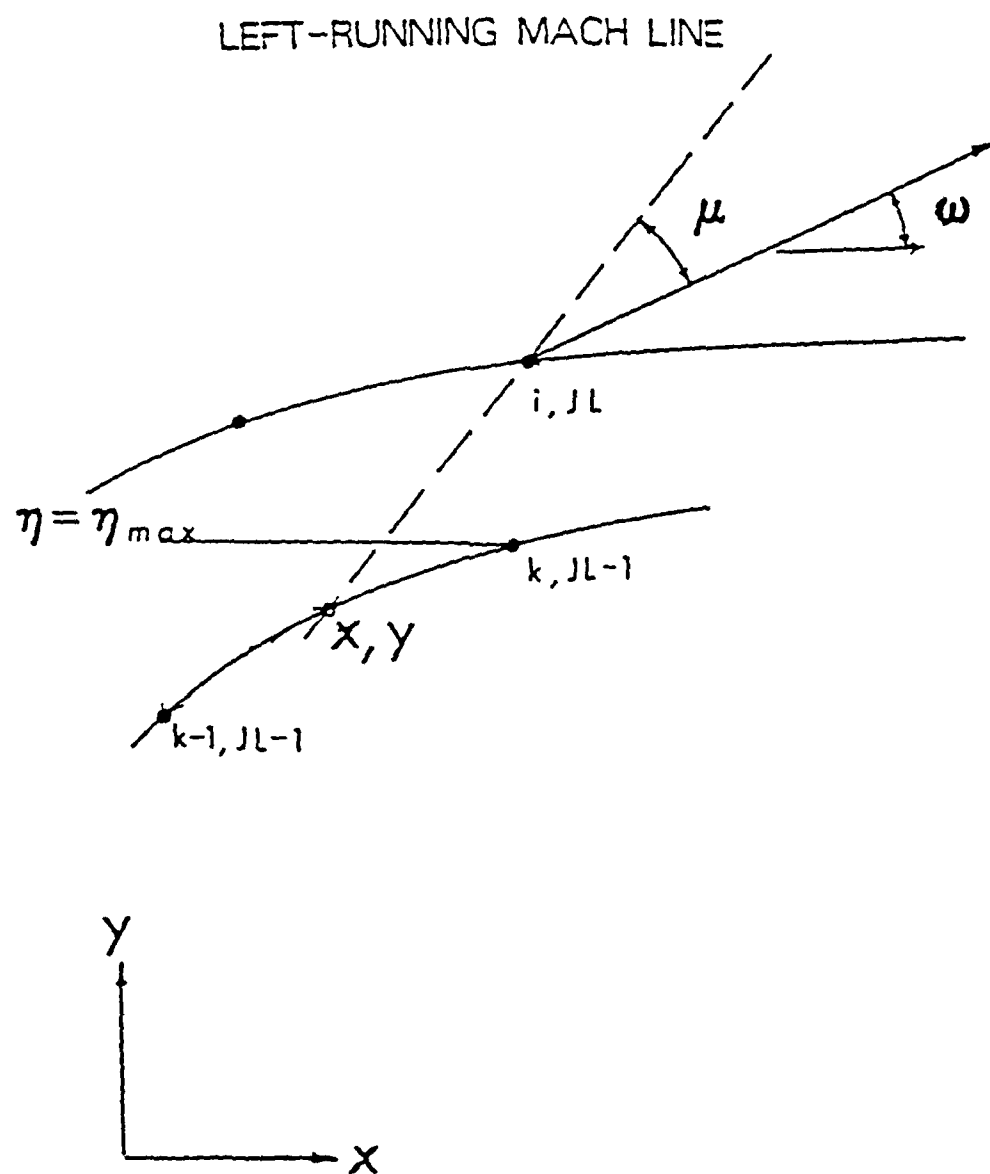$$B = (\Delta x^2 + \Delta y^2)^{1/2}$$

LEFT-RUNNING MACH LINE

Figure A1. Non-reflecting outer boundary condition

(THIS PAGE WAS INTENTIONALLY LEFT BLANK)

No of
Copies Organization

1   Office of the Secretary of Defense
     OUSD(A)
     Director, Live Fire Testing
     ATTN: James F. O'Bryon
     Washington, DC 20301-3110

2   Administrator
     Defense Technical Info Center
     ATTN: DTIC-DDA
     Cameron Station
     Alexandria, VA 22304-6145

1   HQDA (SARD-TR)
     WASH DC 20310-0001

1   Commander
     US Army Materiel Command
     ATTN: AMCDRA-ST
     5001 Eisenhower Avenue
     Alexandria, VA 22333-0001

1   Commander
     US Army Laboratory Command
     ATTN: AMSLC-DL
     Adelphi, MD 20783-1145

2   Commander
     US Army, ARDEC
     ATTN: SMCAR-IMI-I
     Picatinny Arsenal, NJ 07806-5000

2   Commander
     US Army, ARDEC
     ATTN: SMCAR-TDC
     Picatinny Arsenal, NJ 07806-5000

1   Director
     Benet Weapons Laboratory
     US Army, ARDEC
     ATTN: SMCAR-CCB-TL
     Watervliet, NY 12189-4050

1   Commander
     US Army Armament, Munitions
       and Chemical Command
     ATTN: SMCAR-ESP-L
     Rock Island, IL 61299-5000

1   Commander
     US Army Aviation Systems Command
     ATTN: AMSAV-DACL
     4300 Goodfellow Blvd.
     St. Louis, MO 63120-1798

No of
Copies Organization

1   Director
     US Army Aviation Research
       and Technology Activity
     Ames Research Center
     Moffett Field, CA 94035-1099

1   Commander
     US Army Missile Command
     ATTN: AMSMI-RD-CS-R (DOC)
     Redstone Arsenal, AL 35898-5010

1   Commander
     US Army Tank-Automotive Command
     ATTN: AMSTA-TSL (Technical Library)
     Warren, MI 48397-5000

1   Director
     US Army TRADOC Analysis Command
     ATTN: ATAA-SL
     White Sands Missile Range, NM 88002-5502

(Class. only) 1   Commandant
     US Army Infantry School
     ATTN: ATSH-CD (Security Mgr.)
     Fort Benning, GA 31905-5660

(Unclass. only) 1   Commandant
     US Army Infantry School
     ATTN: ATSH-CD-CSO-OR
     Fort Benning, GA 31905-5660

1   Air Force Armament Laboratory
     ATTN: AFATL/DLODL
     Eglin AFB, FL 32542-5000

Aberdeen Proving Ground

2   Dir, USAMSAA
           ATTN: AMXSY-D
                 AMXSY-MP, H. Cohen
1   Cdr, USATECOM
           ATTN: AMSTE-TD
3   Cdr, CRDEC, AMCCOM
           ATTN: SMCCR-RSP-A
                 SMCCR-MU
                 SMCCR-MSI
1   Dir, VLAMO
           ATTN: AMSLC-VL-D

53

No. of Copies	Organization	No. of Copies	Organization

8	Commander
	Armament RD&E Center
	US Army AMCCOM
	ATTN: SMCAR-AET-A/Kline
	                        Chung
	                        Kahn
	                        Hudgins
	            SMCAR-CCL-CA/Hirlinger
	                        O'Niell
	                        Miller
	            SMCAR-FSP-A(1)/Bischer
	Picatinny Arsenal, NJ 07806-5000
		2	Ford Aerospace and
			    Communications Corporation
			Aeronautronic Division
			ATTN: Charles White
			            Bud Blair
			Ford Road
			Newport Beach, CA 92658

2	Commander David W. Taylor Naval Ship ATTN: Dr. S. de los Santos Mr. Stanley Gottlieb Bethesda, MD 20084-5000	1	NASA, Langley Research Center Transonic Aerodynamics Division ATTN: Dr. Michael J. Hemsch Hampton, VA 23665
2	Commander US Naval Surface Warfare Center ATTN: Code DK20/Clare Moore Dahlgren, VA 22448-5000	1	Applied Technology Associates ATTN: Mr. R.J. Cavalleri P.O. Box 19434 Orlando, FL 32814

2	Director
	Sandia National Laboratories
	ATTN: Dr. W.L. Oberkampf
	            Dr. F. Blottner
	Division 1636
	P.O. Box 5800
	Albuquerque, NM 87185
		1	United States Military Academy
			Department of Civil and
			    Mechanical Engineering
			ATTN: LTC Andrew L. Dull
			West Point, NY 10996

1	Massachusetts Institute of Technology ATTN: Tech Library 77 Massachusetts Avenue Cambridge, MA 02139	1	University of California, Davis Dept. of Mechanical Engineering College of Engineering ATTN: Prof. Harry A. Dwyer Davis, CA 95616
2	Director NASA Ames Research Center ATTN: MS-202-1, Dr. T. Pulliam MS-258-1, Dr. L. Schiff Moffett Field, CA 94035		
1	Commandant USAFAS ATTN: ATSF-TSM-CN Fort Sill, OK 73503-5600		

No. of
Copies   Organization

   1   National Tsing Hau University
           Department of Nuclear Engineering
           ATTN: Prof. Ching-Chang Chieng
           855 Kuang Fu Road
           Hsinchu, Taian 300
           R. O. C.

   1   Defense Research Establishment Valcartier
           ATTN: Jon Evans
           P.O. Box 8800
           Courcelette, Quebec
           Canada

(THIS PAGE WAS INTENTIONALLY LEFT BLANK)

USER EVALUATION SHEET/CHANGE OF ADDRESS

This Laboratory undertakes a continuing effort to improve the quality of the reports it publishes. Your comments/answers to the items/questions below will aid us in our efforts.

1. BRL Report Number _____ BRL-MR-3834 _____ Date of Report _____ MAY 1990 _____

2. Date Report Received _____

3. Does this report satisfy a need? (Comment on purpose, related project, or other area of interest for which the report will be used.) _____

_____

_____

4. Specifically, how is the report being used? (Information source, design data, procedure, source of ideas, etc.) _____

_____

_____

5. Has the information in this report led to any quantitative savings as far as man-hours or dollars saved, operating costs avoided, or efficiencies achieved, etc? If so, please elaborate. _____

_____

_____

6. General Comments. What do you think should be changed to improve future reports? (Indicate changes to organization, technical content, format, etc.) _____

_____

_____

_____

	Name
CURRENT ADDRESS	Organization
	Address
	City, State, Zip Code

7. If indicating a Change of Address or Address Correction, please provide the New or Correct Address in Block 6 above and the Old or Incorrect address below.

	Name
OLD ADDRESS	Organization
	Address
	City, State, Zip Code

(Remove this sheet, fold as indicated, staple or tape closed, and mail.)

--FOLD HERE--

BUSINESS REPLY MAIL
FIRST CLASS PERMIT No 0001, APG, MD

POSTAGE WILL BE PAID BY ADDRESSEE

Director
U.S. Army Ballistic Research Laboratory
ATTN: SLCBR-DD-T
Aberdeen Proving Ground, MD 21005-9989

--FOLD HERE--